Journal of Volcanology and Geothermal Research 431 (2022) 107642

Contents lists available at ScienceDirect

Journal of Volcanology and Geothermal Research

journal homepage: www.journals.elsevier.com/journal-of-volcanology-and-geothermal-research

The initial phase of the 2021 Cumbre Vieja ridge eruption (Canary Islands): Products and dynamics controlling edifice growth and collapse

Jorge E. Romero [a,*], Mike Burton [a], Francisco Cáceres [b], Jacopo Taddeucci [c], Riccardo Civico [c], Tullio Ricci [c], Matthew J. Pankhurst [d,e], Pedro A. Hernández [d,e], Costanza Bonadonna [f], Edward W. Llewellin [g], Marco Pistolesi [h], Margherita Polacci [a], Carmen Solana [i], Luca D'Auria [d,e], Fabio Arzilli [j], Daniele Andronico [c], Fátima Rodríguez [d], Maria Asensio-Ramos [d,e], Alba Martín-Lorenzo [d,e], Catherine Hayer [a], Piergiorgio Scarlato [c], Nemesio M. Perez [d,e]

[a] University of Manchester (Department of Earth and Environmental Sciences), Manchester, United Kingdom
[b] Department of Earth and Environmental Sciences, Ludwig-Maximilians-Universität München, Munich, Germany
[c] Istituto Nazionale di Geofisica e Vulcanologia, Italy
[d] Instituto Volcanológico de Canarias (INVOLCAN), 38320, San Cristóbal de La Laguna, Tenerife, Canary Islands, Spain
[e] Instituto Tecnológico y de Energías Renovables (ITER), 38600, Granadilla de Abona, Tenerife, Canary Islands, Spain
[f] Department of Earth Sciences, University of Geneva, Geneva, Switzerland
[g] Department of Earth Sciences, Durham University, Durham, United Kingdom
[h] Department of Earth Sciences, University of Pisa, Pisa, Italy
[i] School of Earth and Environmental Sciences, University of Portsmouth, Portsmouth, United Kingdom
[j] School of Science and Technology, Geology Division, University of Camerino, Camerino, Italy

ARTICLE INFO

Keywords:
Pyroclastic cone
Mafic volcanism
Volcanic instability
Volcano monitoring
Conduit dynamics
Pre-eruptive conditions

ABSTRACT

Tajogaite cone in the Cumbre Vieja ridge (La Palma, Canary Islands) erupted between 19 September and 13 December 2021. The tephra and lava sourced from the newly formed fissure rapidly built a pyroclastic cone. During the early days of eruption and after several small-scale landslides, the west flank of the edifice partially collapsed on 25 September, breaching the cone and emplacing a prominent raft-bearing lava flow. Our research combines direct observations, digital elevation models, thermal and visible imaging, and textural and compositional investigation of the explosive products to describe and characterize the edifice growth and collapse. The cone built over a steep slope (26°) and its failure occurred after an intense phase of lava fountaining (up to 30 m^3 s^{-1}) that produced rapid pyroclastic accumulation. We suggest that an increased magma supply, to an ascent rate of 0.30 m s^{-1}, led to the rapid growth of the cone (at 2.4 × 10^6 m^3 day^{-1}). Simultaneously, the SW lava flow reactivated and formed a lava 'seep' that undercut the flank of the cone, triggering a lateral collapse via rotational rockslide that moved at minimum speeds of 34–70 m h^{-1}. The lateral collapse formed a ~ 200 m wide scar, involving 5.5 × 10^6 m^3 of material, and covered 1.17 km^2 with decametric edifice portions and raft-bearing lava. The collapse produced a modest change in the vent geometry, but did not affect eruptive activity long term. A short pause in the eruption after the collapse may have been favored by rapid emptying of the shallower magma system, reducing ascent rates and increasing crystallization times. These results reveal the complex chain of events related to the growth and destruction of newly formed volcanic cones and highlight hazards when situated close to inhabited areas.

1. Introduction

The formation of small-volume mafic volcanoes (i.e., ≤ 1 km^3; Valentine et al., 2006) may pose significant hazards for nearby inhabited areas. Due to the scarce instrumental observations of their eruptions (e.g., Parícutin 1945 or Eldfell 1973; Williams and Moore, 1983; Luhr and Simkin, 1993; Sumner, 1998) understanding of the processes of growth and destruction of such cones is still limited. The evidence indicates that

* Corresponding author.
E-mail address: jorge_eduardorm@hotmail.com (J.E. Romero).

https://doi.org/10.1016/j.jvolgeores.2022.107642
Received 3 April 2022; Received in revised form 31 July 2022; Accepted 2 August 2022
Available online 6 August 2022

cone-forming eruptions include mild-Strombolian styles (McGetchin and Chouet, 1974) but also intense phases of explosive activity that rapidly accumulate pyroclastic products to form such landforms (e.g. Mannen and Ito, 2007; Kereszturi and Németh, 2012; Romero et al., 2022). Consequently, many pyroclastic cones reach their final heights during the first days of eruption (Wood, 1980). In this respect, resulting steep cone flanks combined with the pre-eruptive topography and the geomechanical properties of the agglutinated deposits may predispose cone instability (e.g., Sumner, 1998; Apuani et al., 2005a, 2005b; Norini et al., 2008; Stewart and Németh, 2009; Kereszturi and Németh, 2012; Hightower, 2016; Romero et al., 2021). The rapid geomorphic changes (e.g., vent reorganization, crater erosion, or lateral lava intrusion; Patrick and Orr, 2012; Calvari et al., 2016) or gentle lava effusion from the base of the cone (e.g., Valentine et al., 2005, 2006; Valentine and Gregg, 2008; Riggs and Duffield, 2008; Báez et al., 2016; Presta and Caffe, 2014; Filipovich et al., 2019; Younger et al., 2019; Marín et al., 2020; Kaneko et al., 2022) may initiate the collapse. Also, magma intrusions conferring repeated thermal stress and mechanical weakening (Andronico et al., 2018a, 2018b; Romero et al., 2021) may also represent efficient triggering factors. Despite most of these collapses are characterized by low velocities, their rapid occurrence may form debris avalanches or pyroclastic density currents (Behncke et al., 2008; Norini et al., 2008) or induce increased explosive activity by sudden decompression of the magma column (Németh et al., 2011; Romero et al., 2020; Cutler et al., 2022). On the other hand, large mounds or rafts of welded, partially welded, or loose pyroclasts (Valentine and Gregg, 2008) including proximally agglutinated material (Holm, 1987) are rafted away from the cone on top of lavas (Valentine and Gregg, 2008; Brown et al., 2015; Andronico et al., 2018a). Hence, studying the eruptive styles and dynamics during cone growth and the factors predisposing and triggering cone collapses is essential for assessing the hazard of cone-forming eruptions, especially during their initial stages of growth.

The 2021 formation of Tajogaite cone in the Cumbre Vieja ridge (La Palma, Canary Islands, Spain) was initially characterized by five days of intense explosive activity before the western flank of the edifice started

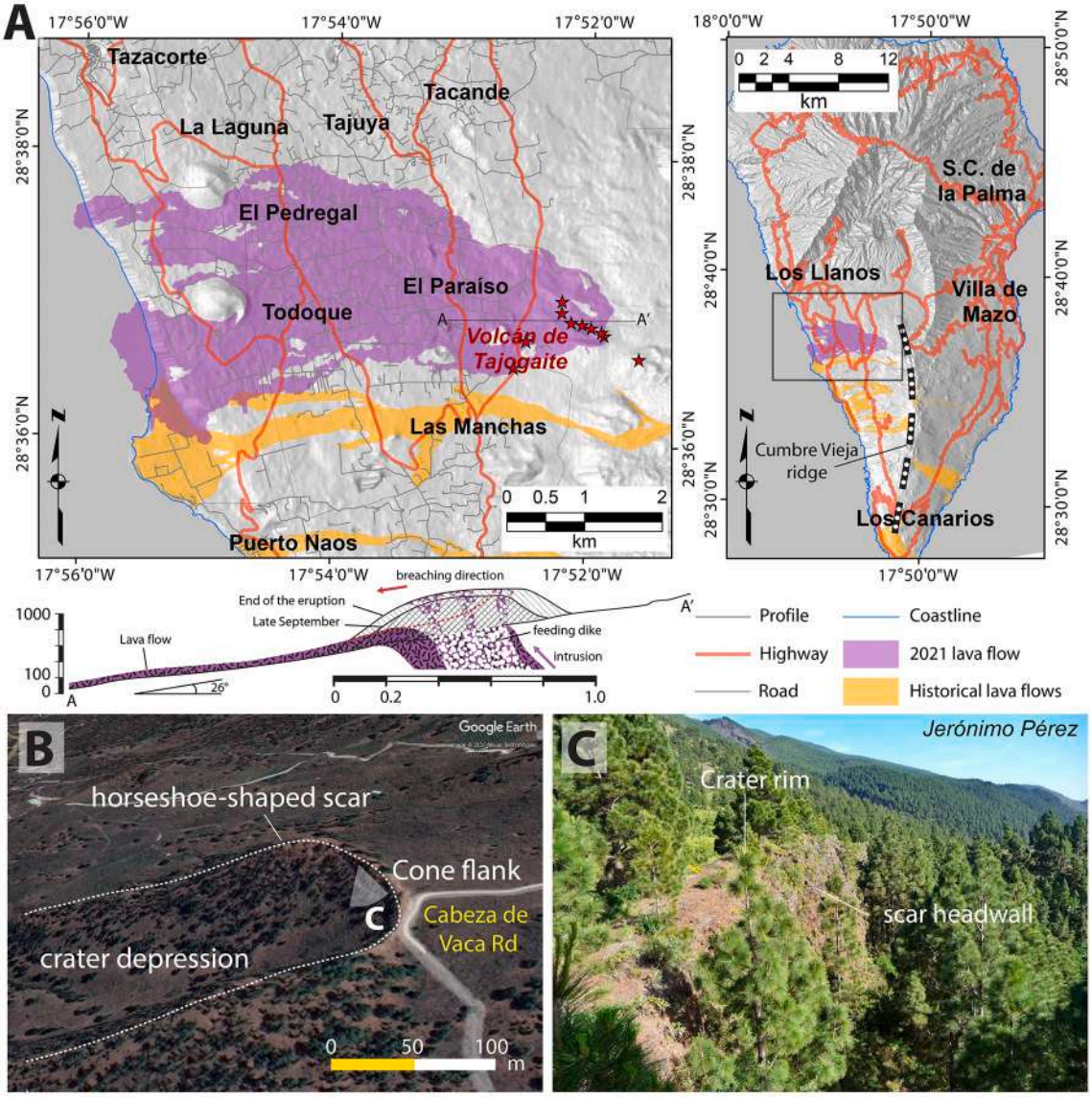

Fig. 1. A ALOS-Palsar hillshade map (12.5 m resolution) of the Tajogaite volcano pre-eruption surface and La Palma island, indicating the eruption vents (red stars) and the lava flow extent by the end of the 2021 eruption, courtesy of the Copernicus Emergency Management Service website (https://emergency.copernicus.eu/) EMRS546 Product 63. The profile indicates the directions of the dike and cone breaching. Historical lava flows are also indicated in orange. B: Pre-eruptive surface and its geomorphologic interpretation as in September 2021 (Google Earth ™). C Photo of the eruption site before the 2021 eruption, showing the remnants of a collapsed pyroclastic cone. (For interpretation of the references to colour in this figure legend, the reader is referred to the web version of this article.)

to collapse. This process was most evident on 25 September, when large sections failed downslope. In contrast to other pyroclastic cone -forming eruptions, even the historical ones in La Palma, the recent eruption occurred in a highly populated area. It covered nearly 12.4 km^2 with lava, burying about 3000 private and public buildings (Carracedo et al., 2022) and entire towns (Fig. 1A). The eruption site provided easy access to viewpoints, allowing the collection of large amounts of regular observations and data. Hence, this eruption offers a rare and unique opportunity of studying the growth and the *syn*-eruptive collapse of a newly formed pyroclastic cone, and its implications for volcanic hazards.

In this contribution, we combine direct observations (on the eruptive activity and cone morphology), digital elevation models acquired with an Unoccupied Aerial System (UAS), and instrumental volcano monitoring (visual and thermal imaging) to reconstruct the first days of the Tajogaite cone formation. In addition, stratigraphic descriptions of the tephra fallout deposits and analysis of a time series of samples covering the pre- and post-collapse stages are analyzed focusing on the pyroclastic textures and compositions. We offer a comprehensive interpretation of the eruption dynamics and mechanisms behind lateral collapse. These results also offer a complete framework for the occurrence of lateral collapses and their related hazards at small-volume mafic volcanoes.

1.1. Cumbre Vieja ridge: recent activity and the 2021 eruption

The Canary hot-spot archipelago is one of the most active volcanic regions of the planet (Abdel-Monem et al., 1972; Carracedo et al., 1998). La Palma is the most historically active of the Canary Islands, with the Cumbre Vieja ridge having sourced eruptions in 1585, 1646, 1677–1678, 1712, 1949, 1971; Guillou et al., 1998; Carracedo et al., 1998; Klügel et al., 2000; Carracedo et al., 2001; Casillas et al., 2020). These eruptions were all fed by multi-vent fissure systems, each erupting between 10 and 80 $\times$ 10^6 m^3 of lava and pyroclasts (Klügel et al., 2000; Day et al., 2000; Longpré and Felpeto, 2021). The new eruption in the Cumbre Vieja ridge began on 19 September 2021 after intense seismic unrest, geochemical anomalies, and deformation that initiated as early as 2017 (e.g., Torres-González et al., 2020; Padrón et al., 2021; Carracedo et al., 2022; Civico et al., 2022a; D'Auria et al., 2022; Pankhurst et al., 2022). Erupted products consisted mainly of lava and tephra of tephrite/basanite bulk composition (Carracedo et al., 2022; Pankhurst et al., 2022). Compared to the two most recent eruptions in La Palma (e.g., San Juan 1949 and Teneguía 1971; Klügel et al., 2000; Barker et al., 2015; Longpré and Felpeto, 2021), Tajogaite 2021 had the longest

Fig. 2. Chronology of the eruption's first phase. A: Strombolian activity and active lava front (c. 3 m-high) towards the SW. B: Growth of the volcanic edifice by 24 September. Strombolian activity occurred at the main vent, and the SW lava flow static, allowing rapid pyroclastic accumulation. C: Main vent lava fountaining on 24 September around 9 pm (lt), courtesy of Miguel Calero. The N vent sourced effusive activity. D: Cone morphology on 25 September, showing two simultaneously active vents sourcing lava fountains. E: Breached morphology of the edifice on 26 September afternoon, showing a reactivation of the SW lava flow carrying rafts on top, together with explosive lava fountaining with high production of tephra. F: Cone regeneration on 28 September. The main vent developed explosive active with ash-laden columns, while the post-collapse vent is quiet. G: Opening of multiple vents along the fissure by 01 October. The highest vents located southwest produced explosive activity, while the lower vents were effusive.

duration and the largest eruptive volume.

The formation of Tajogaite cone began on 19 September 2021, with the opening of a fissure around the Cabeza de Vaca, 1.6 km NE of the neighborhood of El Paraíso (Fig. 1A). The fissure initially consisted of five vents aligned ~N60° W which opened between 840 and 1100 m a.s.l. (Fig. 1A). The pre-eruptive substratum consisted of a conic structure with a ~ 200 m-diameter U-shaped summit opened W, forming an inclined surface with a ~ 26° slope angle facing W (Fig. 1B). The pre-eruptive ground observation of this area indicates the pre-existence of coarse, bomb-sized and well-preserved pyroclastic ejecta in the crater rim and a decametric scar headwall exposing proximal pyroclastic successions (Fig. 1C), which suggests the eruption site occupied part of a small (~50 m-high) pyroclastic cone breached to the W. In fact, in the map of Carracedo et al. (2001), this structure has been recognized as a pyroclastic cone assigned to post-Last Glacial Maximum age.

During the first days of eruption, the explosive activity consisted of alternating lava fountains (Fig. 2A) and "rapid" Strombolian explosions (i.e., periods of increased frequency of Strombolian explosions, Houghton et al., 2016; Fig. 2B). Throughout the eruption 'a'ā lava flows drained to the west. Between 21 and 24 September, long-lasting fountaining episodes (i.e. several minutes to hours) became more frequent, while simultaneous lava effusion and sporadic Hawaiian fountaining occurred from the N flank vent (Fig. 2C). The pyroclastic edifice grew up rapidly to ~130 m high (Fig. 2B) around a main vent of the erupting fissure, that produced most of the eruptive activity (Fig. 2B). Several small-scale landslides occurred during this period.

The edifice then experienced a dramatic lateral collapse on 25 September (Fig. 2D), which involved part of the cone's west flank. At 13.52 LT (local time, GMT +1), the cone breaching formed a U-shaped collapse scar that opened to the W-SW (Fig. 2E); the activity was mostly concentrated in a vent lying directly to the west of the main vent, sourcing two lava fountains (Fig. 2D). Later in the afternoon, two inclined, 50–100 m-high lava fountains were visible within the collapse depression, and the N flank exhibited Hawaiian fountaining (Fig. D).

After the collapse, volcanic activity persisted with no significant changes; however, a complete pause in the activity, concomitant with a drop in tremor for about 10 h, occurred on 27 September; soon afterwards, explosive activity resumed at the main vent (Fig. 2F). Days after, on 1 October, the fissure architecture was well-defined and a decoupling in the vent activity was observed. An upper southernmost set of vents produced mostly explosive activity; it generally included a main vent having Strombolian activity, and intermittent lava fountaining (~250 m high) produced ash columns varying from 1.6 to 2.7 km in height above the vent. Sporadic gas jetting occurred in the southeast vent and the lowermost northwest vents sourced effusive activity (Fig. 2G) and Hawaiian fountaining.

After 11 October, activity changed to a phase of variable intensity, characterized by the interplay between ash-laden Strombolian columns (Fig. 2A) and sporadic episodes of lava fountaining, while the opening of new vents produced ash-laden eruption columns (Fig. 2A). Lava effusion continued intermittently from the lowest vents or lateral, short-lived vents around the cone (González, 2022), but it was mainly confined within the channels produced by the earliest effusive activity. The latest stage of the eruption occurred on 13 December around 18:20 LT, when a strong eruption produced a column of 8 km in height (Fig. 2A). The column was sustained almost continuously for more than one hour.

2. Methods

2.1. Remote and direct observations of the activity

We carried out visual observation of the activity between 24 and 26 September using a fixed surveillance camera (Brinno TLC200 Pro acquiring one frame every 5 s at 1280 × 720 pixels) based in Finca La Cruz (Tazacorte, ~7 km NW from the vent). Video processing consisted of extracting the red channel from the original colour frames and computing its maximum row-wise and column-wise for each frame. From the same location, the cone and the eruptive activity were filmed at 25 frames per second and 3840 × 2160 pixels resolution, using a Sony AX100 camcorder. Pixel scale at the vent distance was either calculated from the known optical parameters of the cameras or derived from the known projected size and distance of objects within the camera field of view. In parallel, thermal camera infrared images were captured every 15 min from Camino El Pedregal (La Laguna, Los Llanos de Aridane, ~3.3 km WNW from the vent). We used a ©FLIR A655sc camera with FOL25 lenses, NOF filter and sensitivity range from 100 to 650 °C calibrated to atmospheric temperature and humidity to 20 °C and 65%, respectively, and objects emissivity to 0.95.

Ground-based visual and thermal observation was integrated with UAS remote surveys. We acquired over 1500 aerial pictures using a DJI Mavic 2 Pro equipped with a 1" CMOS 20MP sensor and a 28-mm (35-mm equivalent) focal length lens. UAS overflights of the lava field were carried out on 26 September (survey completed at 13.30 LT) and of the cone on 27 September (survey completed at 16.50 LT), when the pause in the eruptive activity permitted UAS operations on the cone area, inaccessible in the previous and following days. We flew the UAS 50–350 m above ground level with both nadir and oblique camera angles to collect GNSS information and aerial images to compile digital terrain models and orthomosaics (see Supp. Material 1 for details). We generated a 0.5 m/pixel DSM and a 0.1 m/pixel orthomosaic, covering an area of about 4.5 km^2 (Civico et al., 2022).

2.2. Field observations and sampling

Field observations of the eruptive activity and its resulting deposits were carried out between 20 September and 20 October, 11–19 November 2021, and January–February 2022. These activities included drawing an isopach map of the tephra fallout based on 70 sites visited and constantly updated until 11 October, along accessible roads in the central and southern areas of La Palma Island. These isopachs were integrated using AshCalc V.1.1 (Daggitt et al., 2014) to compute volume estimates using the Weibull method (Bonadonna and Costa, 2012) (see Supp. Material 2 for details).

Individual tephra beds were discriminated based on their thickness, internal structures, and textures (e.g., grading). Eight stratigraphically controlled tephra samples from the lowermost tephra unit (LU) were collected. These are associated with distinct layers (LU1.2, LU1.4, LU1.6, and LU2), both at the Llano del Jable Astronomical Viewpoint, 1.3 km NE from the fissure, and at Camino San Nicolas, 1.2 km SE, where the full stratigraphy of the deposit was retrieved. From dry samples we performed grain size analyses between 2 to −4 phi ($phi = -log_2 d$; d is the particle diameter in mm) at regular steps of 1 phi, except phi 0. Largest and most representative (i.e., most abundant) juvenile clasts were also picked from the same four samples. In addition, geologic observations were carried out on the lava flow on 10 October for the recognition and description of the rafted blocks produced during the collapse event.

2.3. Analytical methods

Polished thin sections were produced, two for each sample, totaling 8 representative scoria lapilli clasts (ranging from 10.7 to 17.5 mm^2 each) from samples LU1.2, LU1.4, LU1.6, and LU2.1, in addition to one ash fall sample collected on 30 September at Santa Cruz de La Palma port (~12.2 km NE from the vent). According to eyewitness accounts, this tephra was deposited on 25 September. Petrographic descriptions were carried out using a polarized light microscope. Thin sections and individual ash size particles of each sample were carbon-coated and analyzed with the FEI Quanta 650 FEG-SEM electron microscope (Department of Earth and Environmental Sciences, University of Manchester) operated at 10 to 15 kV (for ash grains and polished thin sections, respectively), beam current of 10 nA, and working distance of 10

mm. We collected 33 semi-quantitative geochemical maps of mineral phases and 25 backscattered electron images (BSE) from thin sections with areas of 0.006 and 1.2 mm^2 through electron dispersive X-Ray spectroscopy (EDS).

Bulk-rock chemical compositions of lava and lapilli prepared as 32 mm pressed pellets were analyzed carried out using the Rigaku NEX-CG Energy Dispersive X-ray fluorescence (ED-XRF) in the Geography Department at the University of Manchester. The results were calibrated against the USGS BHVO-2 and only major elements are reported (see Supp. Mat. 1 for details).

Chemical compositions of glass, crystals and melt inclusions were obtained using the Cameca SX100 electron microanalyzer probe (EPMA) housed in the Department of Earth and Environmental Sciences at LMU Munich, Germany. The calibrated measurements were acquired at 15 kV acceleration voltages, 5 nA beam current and 1 or 5 μm beam spot sizes for crystal and glass compositions, respectively (see Supp. Mat. 1 for details). From crystal core-rim and glass data we estimated the pre-eruptive temperatures and pressures using clinopyroxene-melt equilibrium (Neave and Putirka, 2017) together with plagioclase-melt equilibrium thermobarometry (Putirka, 2008). Equilibrium conditions are $K_D(Fe-Mg)^{cpx-liq} = 0.28 \pm 0.08$ and $K_D(An-Ab)^{pl-liq} = 0.27 \pm 0.11$ for $T \geq 1050$ °C. Caution is required for clinopyroxene-melt data because it has not been calibrated for highly alkaline systems, potentially resulting in pressure overestimation. In the absence of direct H_2O measurements, we use 1 wt% water content (Kovalenko et al., 2007), also constrained from the Cumbre Vieja historical products (Weis et al., 2015). Pressures were converted to depths (see Supp. Mat. 1 for details).

3. Results

3.1. Eruptive activity during the collapse event

Between 03:00 and 06:00 LT on 25 September, a 250 m-height lava fountaining from the main vent deposited incandescent material on the W flank of the edifice; simultaneously, rolling blocks and/or clastogenic lava formed to the SW (Fig. 3A). Between 06:18 and 08:09 LT, the discharge into the SW lava flow increased rapidly and the edifice failed to the SW (Fig. 3A). Soon after (08:18 LT), lava overflow occupied all the W side of the cone, transporting decametric rafts from the top of the edifice (Fig. 3A). The intense fountaining activity (Fig. 3B) persisted within this period with no change, as before the collapse. The processing of the red colour signal from steady footage (Supp. Video 1) confirmed no significant change in the lava fountain height before and after the collapse (Fig. 3A). We observed that the collapse event was accompanied by the opening of a new vent with lava fountaining activity and the overflow of the lava sourced from the N vent (Supp. Video 1). Subsequent activity rapidly rebuilt the cone eventually masking the collapse scar.

3.2. The 25 September collapse event

Based on the morphometric analysis of 2-D video footage captured during the cone lateral collapse, we observed the progressive transport of the largest main block of the flank (Fig. 4A; Supp. Video 2). At 07.14 LT, some smaller landslides occurred in the upper part of the cone, indicating the beginning of the collapse. The changes in the vertical and horizontal position of the main block indicate the movement progressed at least in two different stages: the first lasted at least 1.4 h and had a minimum apparent velocity in the horizontal axis of $v_h = 24$ m h^{-1} while

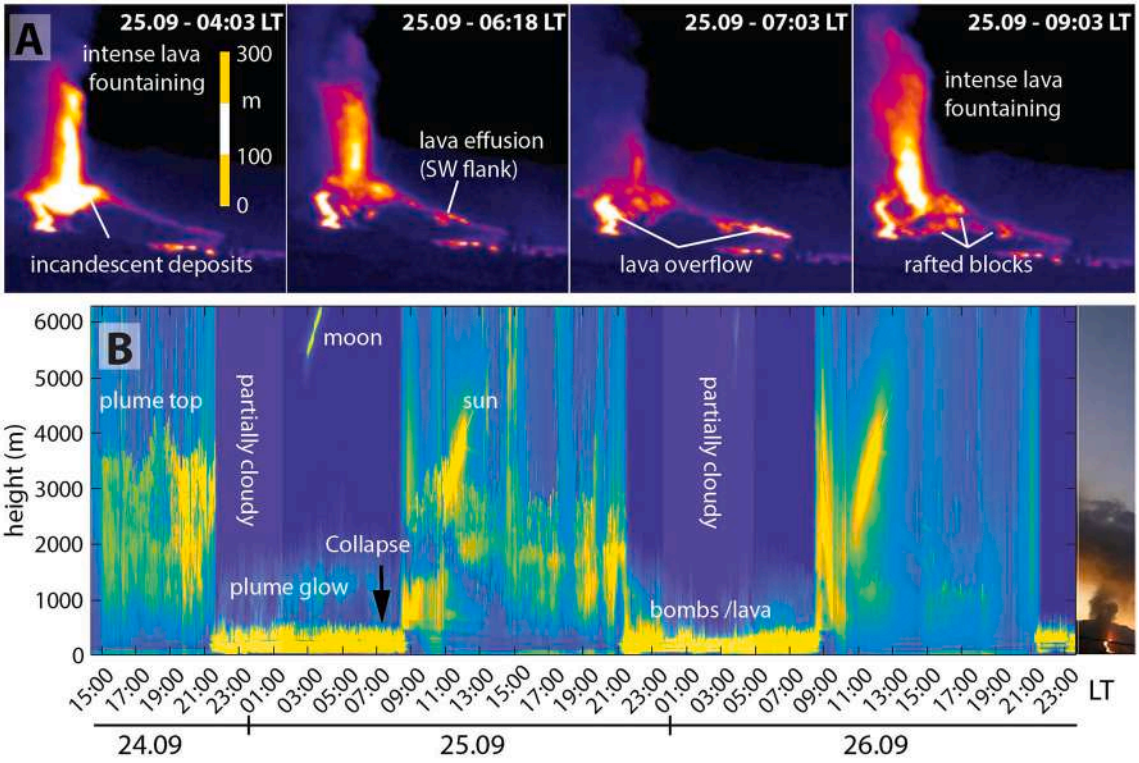

Fig. 3. Main edifice collapse during the Tajogaite 2021 eruption. A: Thermal imaging sequence of the pre- and *syn*-collapse evolution of the eruptive activity seen from Camino de la Gata, 3.3 km WNW from the eruption. The sequence shows lava outburst to the NW and SW during the collapse, followed by the initiation of block rafting. B: Time evolution of the maximum of the red colour component of the video along the vertical direction (region of interest is appended to the right of the plot) from 15:00 of 24 Sept. to 23:00 of 26 Sept. 2021 (lt). The projected height of the top of the plume, the plume base, and the incandescent bombs and lava are visible to different degrees in daylight and at night-time. (For interpretation of the references to colour in this figure legend, the reader is referred to the web version of this article.)

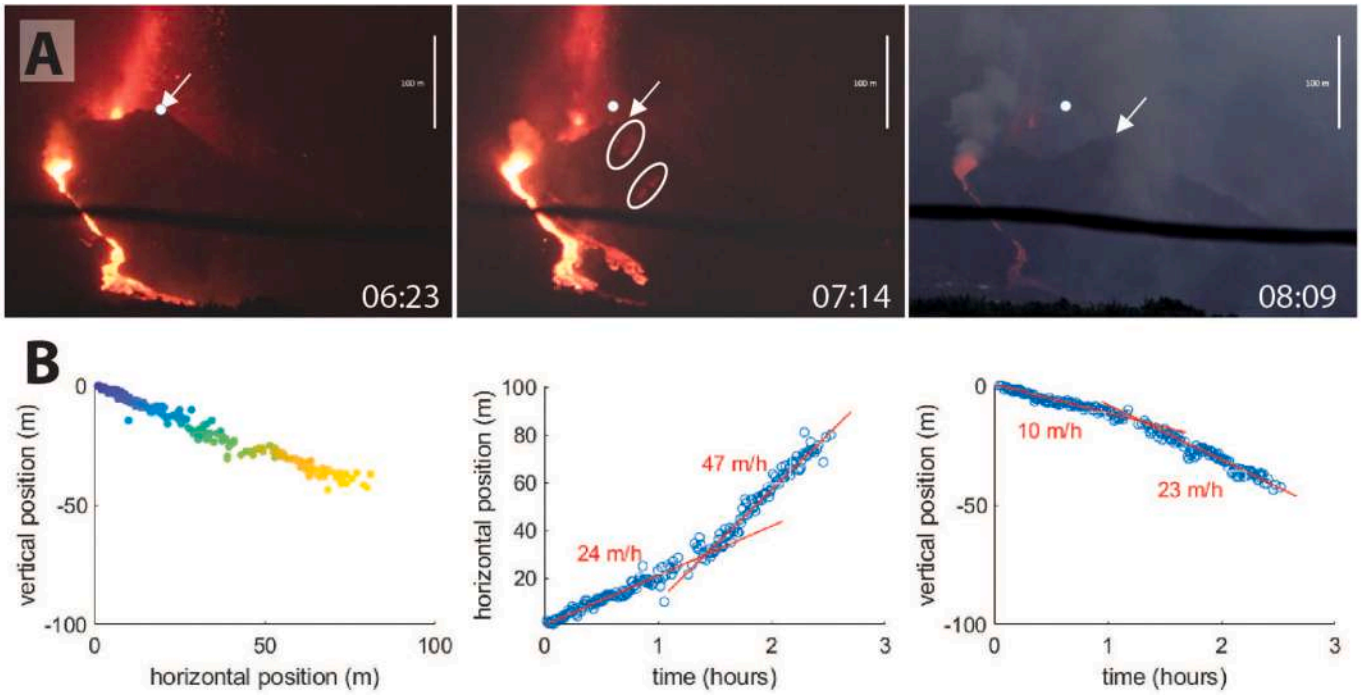

Fig. 4. Kinematic observations of the proximal block rafting. A: Still frames from a video collected from Finca La Cruz (Tazacorte), ~7 km. from the vent. White dot and arrow mark a reference point and its displacement over time. Dashed ovals encircle landslides on the collapsing flank of the cone. Scale bar is 100 m long at the vent. B: Manual tracking of the point indicated by the arrow in the upper panel. Left-hand panel: over the whole video the point moved almost linearly 81 m westward (right) and 42 m downwards (apparent displacement, projected on a plane perpendicular to the line of sight). The colour key shows increasing time from blue to yellow. Middle- and right-hand panels: The horizontal and vertical apparent displacement of the tracked point over time. (For interpretation of the references to colour in this figure legend, the reader is referred to the web version of this article.)

the second lasted at least 1 h and 20′ and the speed is estimated at $v_h =$ 47 m h^{-1} (Fig. 4B). The vertical velocities for these stages are estimated at $v_v = 10$ and $v_v = 23$ m h^{-1}, respectively (Fig. 4B). Then, the minimum collapse velocity increased after 07:41 LT from $|v| = 26$ to $|v| = 52$ m h^{-1} (considering $|v| = \sqrt{{v_h}^2 + {v_v}^2}$). Small-scale velocity fluctuations may be masked by the tracking resolution.

The UAS-derived DSM and orthophoto (Civico et al., 2022) shows the sequence of effusive stages and morphological changes on the edifice related to the collapse (Fig. 5A). On 26 September, a northern main branch of the lava flows extended up to 3.7 km W from the main vent (Fig. 5A), while a southern branch merged with it at 2.6 km W. The total area covered by lava was 1.9 km^2 on 24 September. A U-shaped scar characterized the collapsed edifice; it had 215 m width by 450 m length (Fig. 5B). Considering the original cone as having an elliptical cross section and a volume of 14.87 × 10^6 m^3, and a crater with a negative volume of 0.46 × 10^6 m^3, the pre-collapse volume reached 14.45 × 10^6 m^3. Hence, the cone formed at a rate of ~2.41 × 10^6 m^3 day^{-1} before the collapse. The volume of the DSM-computed post-collapse cone on 27 September was 8.91 × 10^6 m^3, thus the collapse would have involved 5.54 10^6 m^3 (Civico et al., 2022).

During the collapse, the southern branch of the flow drained part of the collapse material, carrying abundant rafts and producing cataclastic ash by shear between blocks (Fig. 5C). Internally, the rafts consisted of crudely bedded, alternating spatter agglutinate, slightly welded cauliflower bombs, and partly welded coarse lapilli and bombs with an ashy matrix (Fig. 5D). These blocks prevented further lava drainage to the NW, allowing the emplacement of post-collapse raft-bearing lavas to the SW which covered 1.05 km^2 (Fig. 5A). Also, the morphology made by an older, small pyroclastic cone SW from the active edifice shielded some areas preventing lava emplacement (Fig. 5E). Most rafts were localized to the margins of the flow (Fig. 5F), forming prominent lateral levees which reached up to 30 m height and 60–90 m width, developing steep talus of 30–50° slope (Fig. 5F), while the central flow was 30 to 80 m wide being narrower closer to the vent. Some lava lobes at the flow fronts were principally composed of rafted material, thus indicating that a great proportion of the rafts were carried on top the flow to the terminal fronts. Some of the largest fragments of the edifice reached up to 20 m in size and lie closer to the edifice (~1.1 km W; Fig. 5G), while massive megablock accumulations were deposited to the opening of the scar, covered ~0.12 km^2 and extended up to 0.9 km downslope in the collapse direction (Fig. 5B). This flow was active on the morning of 25 September, as seen from an aerial footage courtesy of the Instituto Geológico y Minero de España (IGME, https://youtu.be/PoZA0FqCwEM). The rafts were rapidly buried under the thickening tephra fall deposits (Fig. 5F).

3.3. Tephra deposits

The total deposit stratigraphy consists of three different units: Lower Unit (LU), Middle Unit (MU) and Upper Unit (UU; Fig. 6A). LU consists of lapilli-size beds intercalated with fine-to-coarse ash beds. MU is fine-to-coarse ash dominated with intercalation of lapilli beds, and the UU is mostly made of lapilli-size clasts. UU forms two gray, medium-to-coarse lapilli beds on top of the sequence. According to visual observations of the tephra fallout, in addition to our periodic control at the same stratigraphic stations between October 2021 and February 2022, LU mostly deposited between 19 September and 11 October. We describe LU as covering the pre-, *syn*- and post-collapse stage, while a full description of the stratigraphy, componentry, grain size and distribution of each unit is provided in a companion contribution merging all the work made on the tephra deposits carried out by the various teams and coordinated by INVOLCAN.

From base to top, LU starts with a dark brown ungraded fine-to-medium lapilli bed (LU 1.1; Fig. 6A). LU 1.2 is a clear brown, massive medium lapilli tephra bed. LU1.3–1.5 are a sequence of two clear brown medium-to-coarse ash beds containing scattered fine lapilli, with and a

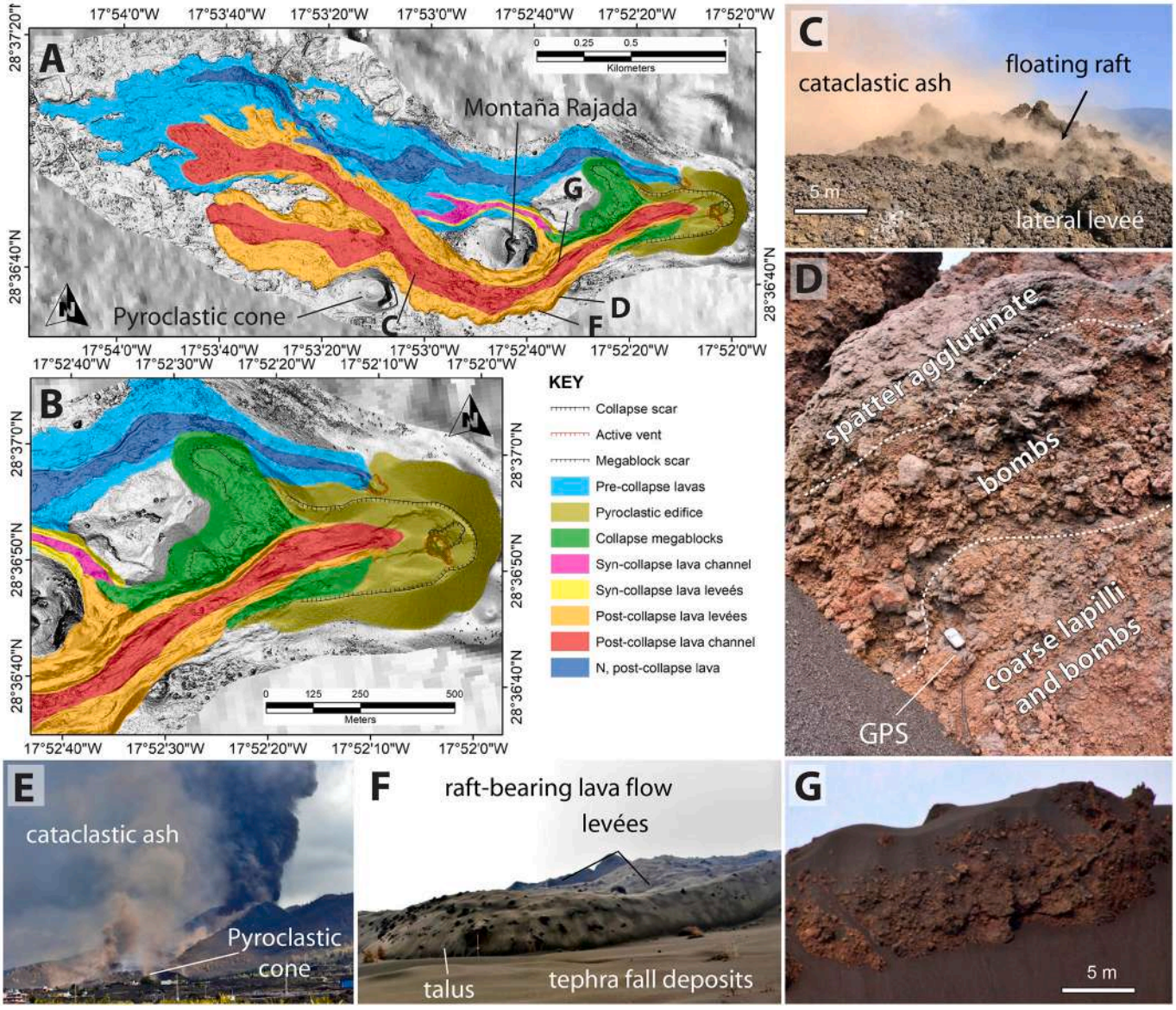

Fig. 5. Deposits resulting from the 25 September lateral collapse. A: Orthomosaic (10 cm resolution) generated from UAS imagery of the lava flows and collapse deposits near the vent. The location of insets is indicated. B: Detail of A indicating the proximal collapse deposits. C: Rafted blocks and cataclastic ash produced by shearing. D Internal architecture (cone beds) in a rafted block (photo acquired on 10 October). GPS (10 × 6 cm) is indicated as scale. E: Cataclastic ash on 25 September as seen from the S (Las Manchas) and pyroclastic cone preventing further lava drainage to the S. F: Morphology of the southernmost 25 September lava flow lobe as seen on 10 October; two lateral levées form steep-sided talus, and rafts emerge all around from the tephra blanket. G: Decametric megablock lying on top of the lava flow.

horizon of gray fine-to-medium lapilli scoria in the middle (Fig. 6A). Upwards, another inverse-to-normally graded bed of brown scoria varying from medium to coarse lapilli represents a period between 23 and 25 September (LU 1.6; Fig. 6A). The uppermost segment of LU consists of inverse-to-normally graded bed of gray medium-to-coarse lapilli beds (LU2.1-LU2.4; Fig. 6A) and ash layers intercalated with fine lapilli scoria to the top (LU3; Fig. 6A). Field inspection indicates that LU2.1 was deposited after the 25 September lateral collapse. The lithologic components from unit LU1.2 to LU2.1 correspond to sideromelane (74–96%) and tachylite (3–11%) plus lithics (1–18%) and free crystals (<2%) showing unsystematic variations; sideromelane is generally brown to golden and tachylite is usually gray or iridescent black.

In terms of grain size, the samples collected both upwind (NE) and downwind (SW) from the fissure displayed unimodal distributions and are poorly sorted, fine-to-very-fine skewed, and contained coarse ash to medium-to-coarse lapilli (Fig. 6B).

LU deposit extends NE-SW on the center and S of La Palma Island, displaying observed thicknesses ranging from 1 mm to 70 cm (Fig. 6C). The resulting isopach contours (11) for LU are ellipsoidal to irregular and well constrained by field observations towards the NW, SW, and NE of the newly formed cone (Fig. 6B); wind reworking and frequent rainfalls prevented confident observations towards the SE. The total deposit volume from LU1.1 to LU2.1 was estimated to be 7.4×10^6 m^3, based on the isopach map, which fitted well with a Weibull distribution for isopach integration (Fig. 6C; Bonadonna and Costa, 2012). From the 70 field control points, only 21 allow visual discrimination of the multiple layer stratigraphy including beds from LU1.1 to LU3, and they correspond to deposits with total thickness between ~1 and 70 cm. These sites are considered to evaluate the average thickness proportion of each layer: LU1.1–1.6 (pre-collapse) corresponds to 78%, from which LU1.6 represents 31% of the total thickness, and LU2.1–3.0 reaches 23%

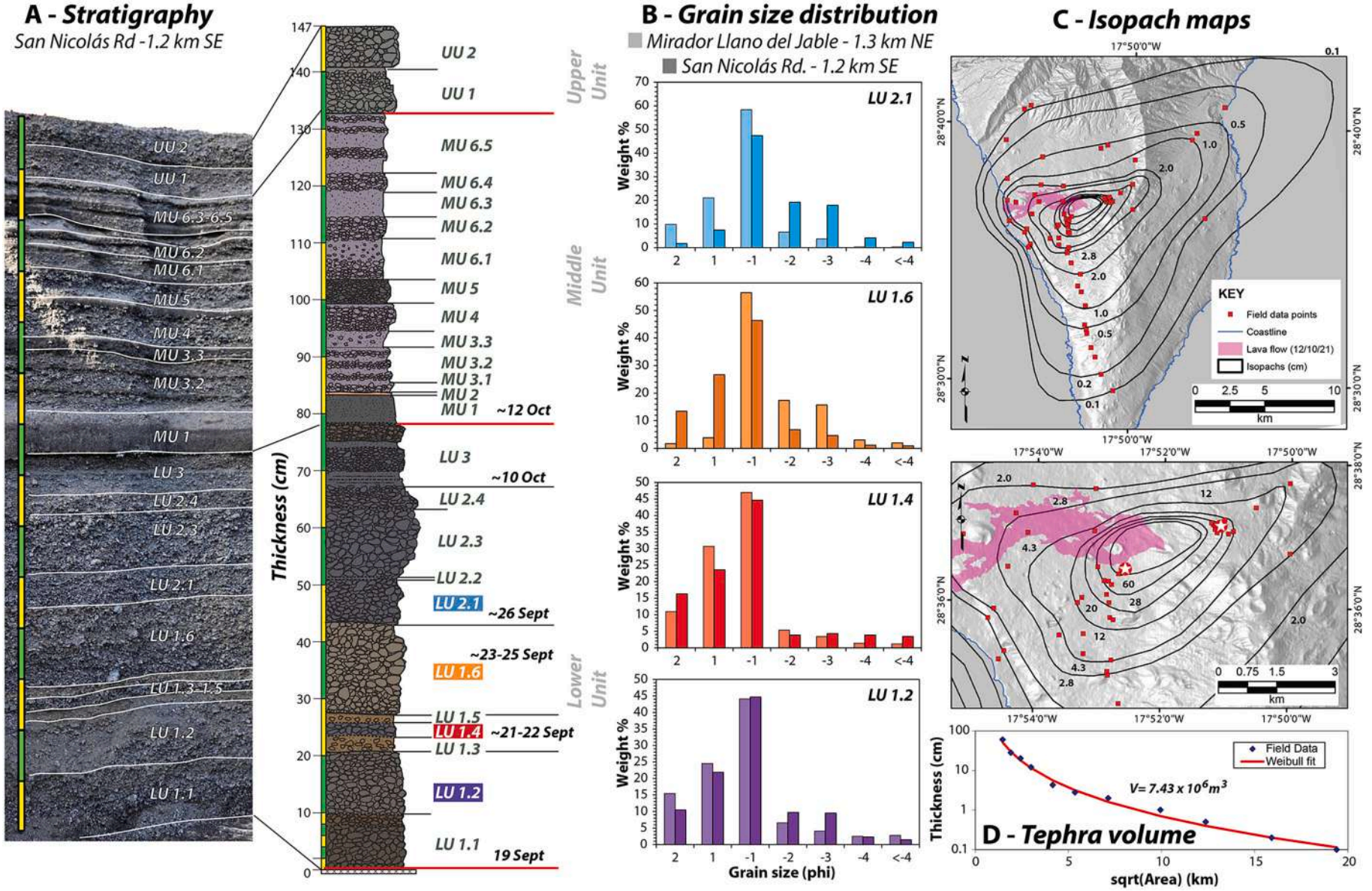

Fig. 6. Tephra fallout deposits between 19 September and 11 October. A: Stratigraphy of the total tephra fallout deposit (as by February 2022) at San Nicolas Rd site (1.2 km SSW from the cone). B: Grain size distribution of selected samples from beds of the Lower Unit at San Nicolás Rd and Mirador Llano del Jable (1.3 km NE) sites. C: General and close-up isopach maps (expressed in cm) of the tephra fall deposit as measured by early October (all layers from LU1.1 to LU2.1). The map contains 70 field control points. Red stars represent the location of sampling for grain size/stratigraphy. Lava flow corresponds to the 12 October situation (https://emergency.copernicus.eu/). D: Thickness (cm) vs square root area (km) regression for the early October 2021 tephra fall deposit integrated using the Weibull method (Bonadonna and Costa, 2012). (For interpretation of the references to colour in this figure legend, the reader is referred to the web version of this article.)

(both post-collapse). Hence, the tephra deposited before the collapse event (i.e. layer LU1.6) accounts for ~2.28 × 10^6 m^3. Accordingly, by dividing these volumes by their corresponding depositional times, we found a higher discharge rate in LU1.6 (~18 m^3 s^{-1}) compared to LU1.2, LU1.3-LU1.5 (~12 and ~ 3 m^3 s^{-1}, respectively) and LU2.1 (~1.4 m^3 s^{-1}) (Supp. Material 2). This is a maximum estimate, as the sub-cm thick total deposit is not considered and mostly represents the events with distal ash transport.

3.4. Mineralogy and textural features of selected scoria

Scoria clasts from units LU1.2 to LU2.1 are highly vesicular glassy particles (i.e., >50% vesicles) with fluidal or blocky shape, smooth surface and occasionally a ragged perimeter (Fig. 7A). Vesicularity ranges from 69 to 79 vol% in samples LU1.2 and LU1.4, while then samples LU1.6 and LU2.1 display 58 and 72 vol%, respectively (Fig. 7B). Vesicles in sample LU1.2 show irregular to subrounded shape and their size varies from 0.03 to 1.7 mm (Fig. 7B). Contrastingly, in samples LU1.4 and LU1.6, vesicles are subrounded or rounded and their size varies from 0.03 to 1.3 mm; vesicle coalescence is incomplete in LU1.4 and is negligible in LU1.6 (Fig. 7B). Sample LU2.1 is similar to LU1.2 as it contains either subrounded or irregular vesicles with sizes between 0.05 and 1.8 mm and these are interconnected (Fig. 7B). Internally, all the analyzed particles correspond to microlite-poor and highly-vesicular scoria (Fig. 7C). However, from the bulk of ashfall deposit correlated to the 25 September collapse, we identify both high- and low-vesicularity particles, the latter with microlite-poor and microlite-rich endmembers (Fig. 7D).

According to the literature, we classify microlites to be those under 0.03 mm (Zellmer, 2021), while larger crystals are phenocrysts. Modal abundances are presented on a vesicle-free basis (Supp. Fig. 1A, B). Glassy groundmass represents between 55 and 65.5% (bubble free basis). From 3-D CSDs of plagioclase crystals we recognized two populations encompassing microlites and microphenocrysts + phenocrysts (Supp. Fig. 1C). Their intercepts and slopes are described in Table 1. The most common mineral phase is clinopyroxene (21–28%); phenocrysts range from 0.3 to 3.4 mm and display subhedral to euhedral shape, sometimes exhibiting embayments. Concentric or patchy zoning with Al-rich cores is frequent in the largest clinopyroxene crystals (Supp. Fig. 2A), and occasionally poikilitic textures with included Fe—Ti oxides or olivine (Supp. Fig. 2B) and apatite are observed. Plagioclase (23–28%) is generally present as scarce euhedral to subhedral phenocrysts (< 1 mm length) but widespread microlites (Supp. Fig. 2C); these are usually tabular, acicular-tabular, or swallowtail. Tabular crystals have rectangular prism shapes. Fe—Ti oxides (5.4–8.0%) usually correspond to subhedral to anhedral phenocrysts and microphenocrysts up to 0.8 mm long (Supp. Fig. 2D). Amphibole varies from 2 to 5 modal % being most abundant in sample LU1.2 and consists of crystals up to 1.7 mm with euhedral or subhedral shape (Supp. Fig. 2E). Olivine is the least abundant (0.7–2.5 modal %) forming euhedral and subhedral crystals ranging from 0.15 to 0.3 mm (Supp. Fig. 2F).

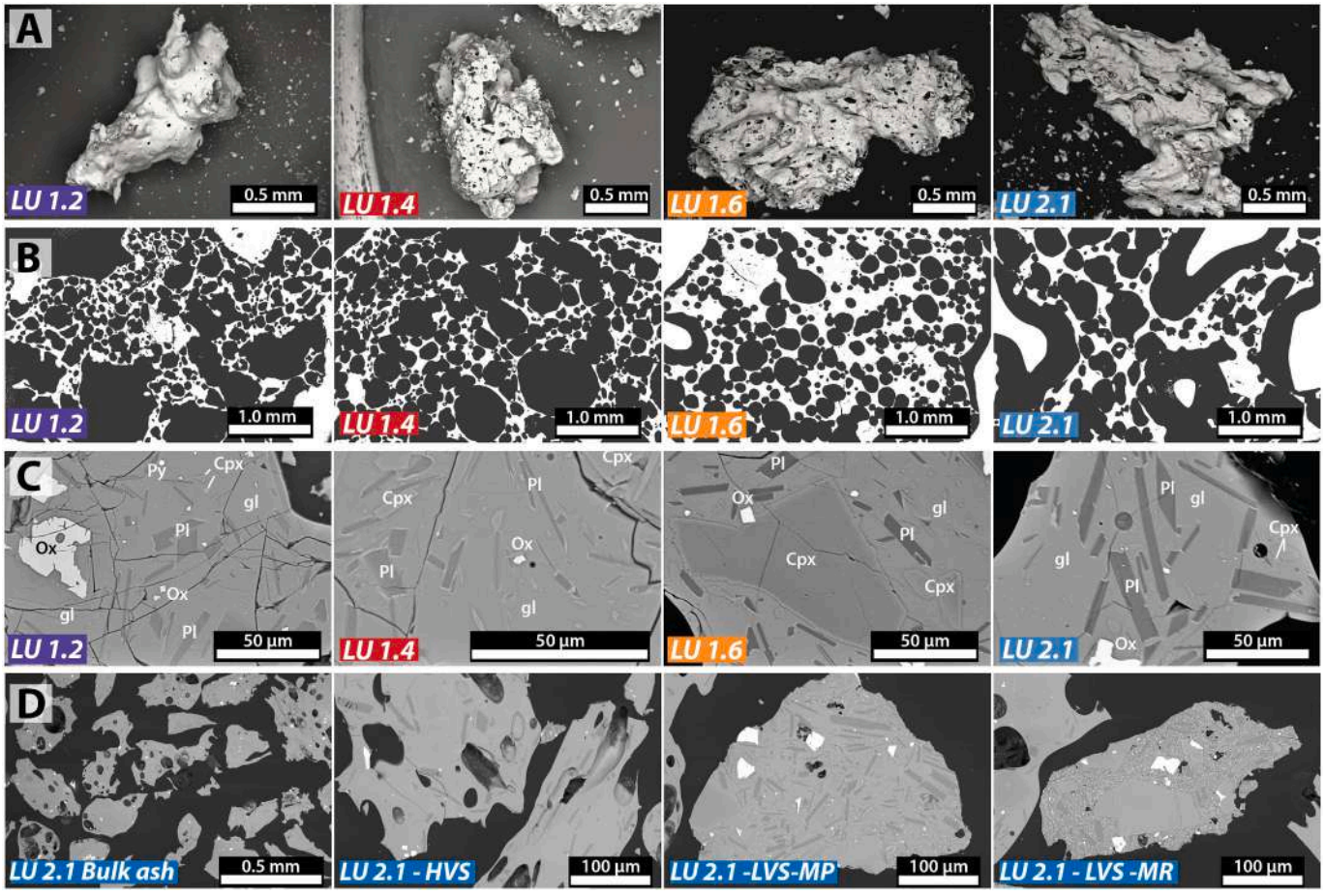

Fig. 7. Textural features of selected pyroclasts (from LU1.1 to LU2.1). A: External texture of individual grains. B: binary images of the studied pyroclasts (black shows vesicles and white groundmass + crystals). C Backscattered electron images of groundmass glass (gl) and microlites (Pl = plagioclase, Cpx = clinopyroxene, Ox = Fe-Ti oxides) in studied pyroclasts. D Different juvenile particles found in the ash erupted on 25 September. HVS = high vesicularity, LVS = low vesicularity, MR = microlite-rich, and MP = microlite poor.

Table 1
Summary of the CSD analysis for samples A to D, with the geometric parameters (slopes and intercepts) of the straight-line regressions obtained from Supp. Fig. 1. Crystallization times are obtained from Eq. (1) and the growth rates from Shea and Hammer (2013) and Arzilli et al. (2015, 2019). Residence times (t_r) are expressed in minimum and maximum values.

		Intercept (mm-4)	Slope (mm-1)	R2	t r min (s)	t r (m)	t r (h)
Microlite	LU1.2	21.878	-259.14	0.92	192.9	64.3	10.7
	LU1.4	18.152	-228.77	0.97	218.6	72.9	12.1
	LU1.6	19.280	-201.89	0.99	247.7	82.6	13.8
	LU2.1	19.031	-220.43	0.85	226.8	75.6	12.6
	LU2.1Ash	18.269	-212.95	0.87	234.8	78.3	13.0
Phenocryst	LU1.2	17.580	-96.38	0.94	518.8	172.9	28.8
	LU1.4	12.933	-58.36	0.98	856.8	285.6	47.6
	LU1.6	15.208	-68.34	0.97	731.6	243.9	40.6
	LU2.1	13.826	-42.66	0.91	1172.0	390.7	65.1
	LU2.1Ash	13.379	-58.17	0.97	859.6	286.5	47.8
Experimental growth rates					Ar2015 (mm s−1)	SH2013	Ar2015 (mm s−1)
					2.00E-05	1.00E-06	1.E−07

3.5. Product composition and initial storage conditions

Both the scoria samples from units LU1.2 to LU2.1 and the lava emplaced from 26 September to 2 October display similar tephritic bulk compositions with high-alkali (7.2 to 8.9 wt% $Na_2O + K_2O$) and low-silica contents (44.8–45.4 wt% SiO_2; Table 2), probably as a result of a crystallization curve (Fig. 8A). These compositions are similar to both lava and tephra sampled reported by Pankhurst et al. (2022), and to lavas sampled by Carracedo et al. (2022) between September and October. The 2021 eruption bulk-rock products contain MgO between 4.2 and 6.7 wt%, displaying a comparatively more evolved composition than the lavas of the Teneguía 1971 eruption (Barker et al., 2015; Fig. 8B). Despite some minor variability in the glass composition towards a more mafic composition from LU1.2 to LU1.6 (Fig. 8C-D), distinctive compositional clusters show that the average glass composition of the products remains broadly constant (Table 2). Sample LU1.6 also displays higher MgO and FeO_t contents but lower alkali ($Na_2O + K_2O$) than the rest of the samples. The latter have comparatively lower FeO_t and higher Al_2O_3 contents than glasses.

The dominant pyroxene composition in LU1.2 is diopside (Fig. 8E; $Wo_{49–51}$- $En_{33–42}$ - $Fs_{11–17}$), and feldspar crystals occupy both anorthite (An_{96}-$Ab_{3.6}$-$Or_{0.1}$) and labradorite fields (Fig. 8F; An_{59}-Ab_{38}-Or_3). In the rest of the samples, feldspars are exclusively labradorites (Fig. 8F; $An_{42–74}$-$Ab_{21–44}$-$Or_{2–17}$). All the plagioclase microphenocrysts and phenocrysts in equilibrium with their melt (Supp. Material 3) inform temperatures between ~1090 and ~ 1116 °C for both rims and cores, while their pressures reach 10.8 to 15.2 kbar (Supp. Fig. 3; Table 3); these have standard errors of ±36 °C and 2.8 kbar (Putirka, 2005, 2008). In the case of clinopyroxene (Supp. Material 3), all the samples except LU1.6 inform temperatures between ~1125 and ~ 1158 °C and pressures from 7.6 to 11.7 kbar. Sample LU1.6 has higher temperatures (~1172–1214 °C) and similar pressures (6.7 to 11.0 kbar) with cores hotter than rims (Supp. Fig. 3; Table 3). Our clinopyroxene-melt results display equivalent pressures and coincident peak temperatures to those reported by Castro and Feisel (2022) for samples collected later in the eruption during November 2021.

4. Discussion

4.1. Factors controlling the cone collapse

Predisposing factors such as topography and rainfall events are usually linked with small-volume lateral collapses (e.g., Romero et al., 2021). The eruption occurred on a 26° inclined surface (Fig. 1A), also occupying the remnants of an already collapsed edifice of Holocene-to-Historic age, thus increasing the gravitational instability of the accumulating incandescent material (e.g., Kereszturi and Németh, 2012; Németh et al., 2011). The "hot" interiors of these materials within the edifice are more readily deformable (e.g., Hightower, 2016) and may act as a low-viscosity, lubricating layer along which basal failure of the scoria cone occurs (Sumner, 1998). No rainfall events contributed to instability during this phase of the eruption.

Among the triggering factors, magma and lava intrusion together with the eruptive rates and rapid cone growth are the most relevant (Romero et al., 2021). First, the dike was not strictly planar in geometry and inclined towards the west-northwest at shallower levels (e.g. De Luca et al., 2022). In this case, the west component is coincident with the direction of the collapse (Fig. 1A). Our stratigraphic observations and tephra quantification also indicate a peaking tephra discharge rate (up to ~18 $m^3\ s^{-1}$) the two days before the date of the lateral collapse (Supp. Material 2) then decreasing to ~1.4 $m^3\ s^{-1}$ in late September-early October. The higher discharge phase of lava fountaining was observed days before and hours after the collapse. Moreover, widespread pyroclastic accumulation was observed by thermal imaging on the W flank, together with the reactivation of the SW lava effusion from the lower flank of the edifice. Increased lava effusion rate also occurred in the N flank vent during the collapse. Hence, increased magma supply through an inclined dike resulted in both lava and tephra erupted at high rates to feed rapid pyroclastic accumulation, whereas basal lava seeping towards the west undercut the edifice through developing a shear plane (Fig. 9). Similar triggering mechanisms have been proposed for other small volume volcanoes in recent and geologically well-preserved collapse successions (e.g., Németh et al., 2011; Kaneko et al., 2022). Also, this is a known mechanism for the collapse of larger stratovolcanoes (e.g., Casagli et al., 2009; Andrade and van Wyk de Vries, 2010). On the other hand, we discard seismicity as a trigger because no significant (i.e., LM

Table 2
Bulk rock and glass geochemistry of selected samples. Bulk compositions were obtained using ED-XRF and those of glass correspond to average values from EMPA measurements.

	Standard	Lava flow / Bulk						Tephra fallout/Bulk				Tephra fallout / Glass		
Sample/Oxide	BHVO-2	CVLP-LF5	CVLP-LF4	CVLP-LF2	CVLP-LF3	CVLP-M9A		CVLP-M1	CVLP-M10	CVLP-BM1	LU1.2	LU1.4	LU1.6	LU2.1
Deposition date		Sep-26	Sep-29	Oct-01	Oct-02	Sept-19/24		Sep-26/Oct-02	Oct-3/5	Oct-16	Sep. 19/20	Sep. 21/22	Sep. 23/24	Sep. 25/27
Lat		28°36.964′N	28°36.851′N	28°37.163′N	28°37.231′N	28°35.514′N		28°38.713′N	28°36.269′N	28°36.577′N	28°37.059′N			
Long		17°54.133′W	17°55.100′W	17°53.082′W	17°53.093′W	17°53.021′W		17°34.025′W	17°52.804′W	17°52.493′W	17°51.193′W			
SiO_2	49.57	44.76	44.83	45.13	45.35	44.77		44.77	44.63	45.00	47.73	47.16	46.07	46.61
TiO_2	2.73	3.81	3.48	3.58	3.55	3.88		3.74	3.68	3.62	3.41	3.60	4.05	3.70
Al_2O_3	13.58	13.54	13.11	13.23	13.11	12.75		12.20	11.86	12.32	16.92	16.55	16.08	16.61
FeO_t	11.82	12.66	12.99	12.51	12.38	12.89		13.34	13.55	13.02	10.10	10.34	11.42	10.54
MnO	0.20	0.24	0.24	0.23	0.23	0.24		0.24	0.25	0.24	0.23	0.21	0.22	0.22
MgO	4.55	4.39	5.35	5.19	5.21	4.83		6.06	6.46	6.19	3.88	3.88	4.19	3.91
CaO	12.38	11.34	11.27	11.39	11.26	11.74		11.88	12.19	11.93	8.62	8.99	9.09	8.90
Na_2O	4.69	7.06	6.82	6.78	6.94	6.61		5.91	5.73	5.99	4.76	5.07	5.01	5.15
K_2O	0.48	1.80	1.68	1.70	1.73	1.90		1.66	1.52	1.57	2.80	2.66	2.54	2.80
P_2O_5		0.42	0.22	0.27	0.25	0.39		0.21	0.15	0.12	1.54	1.54	1.33	1.56
Total	100.00	100.00	100.00	100.00	100.00	100.00		100.00	100.00	100.00	100.00	100.00	100.00	100.00

> 4) earthquakes accompanied the eruption until early 29 September, when deep (17–20 km) earthquakes up to 4.3 LM were first registered (D'Auria et al., 2022).

4.2. Mode of lateral collapse

Our results from the high-definition fixed video camera footage analyses show the flank moving in large, coherent fragments downslope at constant velocities in two periods of time. Analogue models show that continuous edifice growth may trigger shallow-seated, long and narrow collapses (Acocella, 2005). We find these characteristics consistent with our case study as the collapse scar is narrow, U-shaped, and the undercutting did not incorporate basement or subvolcanic rocks; in fact, the transported blocks mainly consisted of subaerial materials deposited near the vent, thus in the external portion of the edifice. Regarding the collapse dynamics, morphological features and triggering factors points to a rotational rockslide (Fig. 9) characterized by the following phases: 1) Pre-collapse stage: lava effusion at the base of the flank acted as a substrate layer being deformed (i.e. a seep; Patrick and Orr, 2012); 2) Syn-collapse stage: a) the movement was initially slow, not instantaneous; b) the deposit was composed of detached proximal slump blocks of decametric dimensions; c) a lava flow carried individual blocks to a greater distance producing raft-bearing flow-parallel ridges (levees); and 3) Post-collapse stage: raft accumulation also occurred at the terminal lobes of the lava flow. This kind of collapse behavior has been previously described in cones formed by rapidly agglutinated spatter or scoria sequences (e.g., Sumner, 1998; Brown et al., 2015). These correspond to complex compound landslides, which reflect a composite movement and failure surfaces consisting of curved and planar elements (e.g., Hungr et al., 2014).

4.3. Eruption style and cone dynamics

From a textural point of view, the dominant eruptive product evolved on a scale of days (i.e., LU1.2 to LU2.1). The higher vesicle fractions of LU1.2 and LU2.1 together with their higher degree of interconnection (i.e., irregular, tortuous and channel-like vesicles) are interpreted as produced by efficient degassing in mafic magmas, while foamy textures as these of LU1.4 and LU1.6 likely represent a late-stage (*syn*-eruptive) nucleation event of the most soluble volatile species (Polacci et al., 2008). The latter have been linked to the fragmentation process responsible of ash formation and quasi-sustained lava fountains at Mt. Etna (Polacci et al., 2009). These interpretations are consistent with the eruption chronology, indicating a transition from Strombolian to rapid Strombolian and almost sustained lava fountaining on 23–24 September, while Strombolian activity seems to resume since 25 September as in sample LU2.1, after the lateral collapse.

We estimated melt and crystal-bearing magma viscosities using the models of Giordano et al. (2008) and Vona et al. (2011). These consider the average temperatures (plagioclase and clinopyroxene geothermometers), glass compositions, and densities of weighted mineral phase proportions (Table 3). Melt viscosity decreases from LU1.2 to LU1.6 (from 37 to 19 Pa s) as a function of increasing temperature and lower silica content, while in the same samples the magma viscosities increase from 2.3 to 14.7 $\times$ 10^4 Pa s due to increasing crystal cargoes (Table 3). Sample LU2.1 yield ~21 Pa s and 3.9 $\times$ 10^4 Pa s for its melt and magma viscosity.

Our CSD plots show a slight curvature, that may reveal pre-existing crystals growing as a separate population during magma ascent (e.g., Brugger and Hammer, 2010; Riker et al., 2015; Cashman, 2020). We use these plots to estimate the different crystallization times of plagioclase using the experimental data of Shea and Hammer (2013) and Arzilli et al. (2015, 2019) as in Bamber et al. (2020) (see Supp. Material 1 for details). For microlites, considering Shea and Hammer (2013) experimental growth rates (Gt) of 1 $\times$ 10^{-6} mm s^{-1}, crystallization times (τ) range between 64 and 82 min (Table 1). The minimum residence time

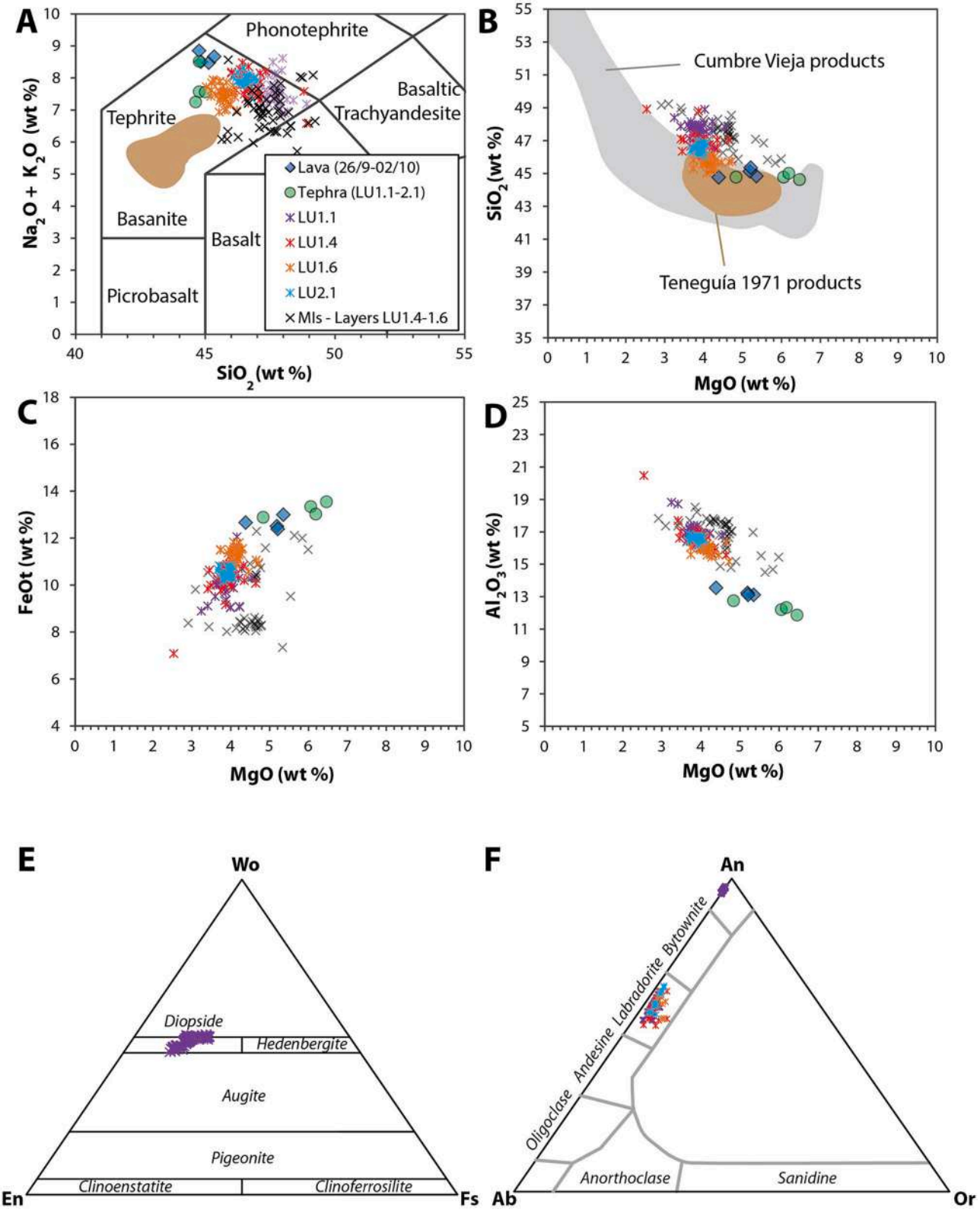

Fig. 8. Geochemistry of the 2021 Tajogaite eruptive products. A: TAS Diagram (Le Bas et al., 1986). Tephra and lava correspond to bulk rock data, and individual beds are groundmass glass compositions. B, C and D are Harker diagrams of SiO_2, FeO_t and Al_2O_3 vs MgO content. Brown and gray fields correspond to the Cumbre Vieja and Teneguía 1971 glass compositions reported in Barker et al. (2015), respectively. E and F are ternary classification diagrams for pyroxene and feldspar, respectively. (For interpretation of the references to colour in this figure legend, the reader is referred to the web version of this article.)

Table 3
Summary of P-T average conditions and viscosity estimates for selected samples. CFV corresponds to crystal volume fraction (total modal %), density represents the weighted values for each crystal phase, and viscosity is calculated for the melt and magma. The melt and crystal-bearing magma viscosities were estimated using the models of Giordano et al. (2008) and Vona et al. (2011). The magma composition is obtained from the the average glass compositions in Table 2.

		Density	Temperature K (crystal cores)			Pressure		Water	Viscosity, Pa s^{-1}	
Sample	CVF	Crystal phase	Pl-liq (Eq. 24a)	Cpx-liq (Eq. 33)	Average	Pl-liq (Eq. 25a)	Cpx (N&P, 2007)	Model H	Melt	Magma
LU1.2	58.4	1950	1370	1407	1389	12.1	9.48	2.2	37.05	2.25E+04
LU1.4	59.5	2027	1371	1420	1396	13.8	9.41	2.1	32.22	3.70E+04
LU1.6	64.1	2152	1372	1474	1423	10.9	9.09	2.0	19.50	1.47E+05
LU2.1	61.5	1881	1373	1419	1396	13.1	9.57	2.2	20.65	3.90E+04

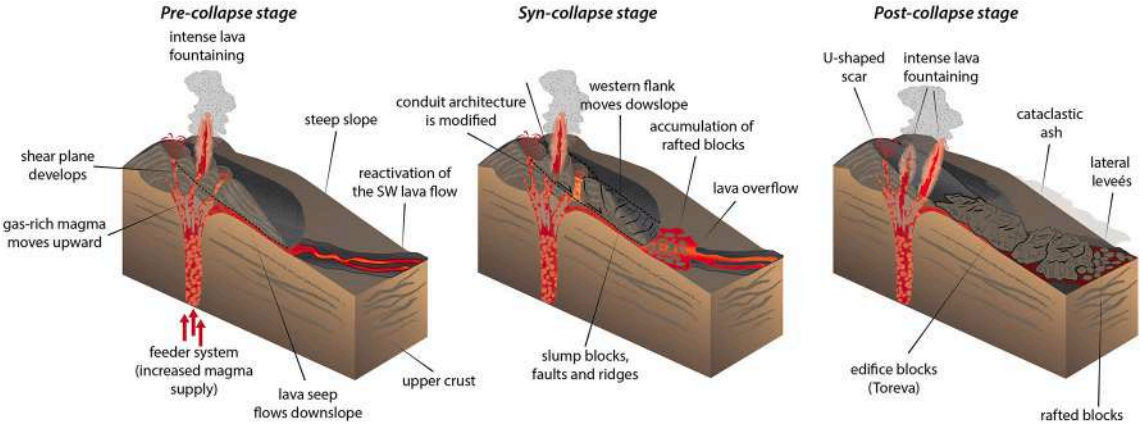

Fig. 9. Cartoon of the 2021 Tajogaite lateral collapse (not to scale). During the pre-collapse stage, the increased magma supply feeds the reactivation of the lava flow to the base of the cone that triggers the spreading and rotational rockslide of the edifice's western flank (syn-collapse stage). The architecture of the vents is modified, and rafts accumulate to the front of the overflown lava. Finally, a new inclined vent sources the lava fountaining and decametric fragments of the edifice are transported to proximal areas (post-collapse stage). Lateral levées are formed and rafts are transported on top of the lava flow.

considering an experimental *Gt* of 1×10^{-5} mm s^{-1} (Arzilli et al., 2019) is 3 to 4 min (Table 1). The shortest τ value is for LU1.2 sample, and the longest is for LU1.6. For phenocrysts, described as a single straight line in crystal population plots (Supp. Fig. 1) we use a rate of 1×10^{-7} mm s^{-1} (Arzilli et al., 2015) and residence times are 28 to 65 h, with the longest times for LU2.1. Then, the increasing temperatures and lowering silica contents together with increasing magma viscosity due to higher crystal cargoes from LU1.2 to LU1.6 may be indicative of an increased supply of deeper magma and the disaggregation of crystal mushes along its pathway to the surface.

To estimate the magma nucleation and ascent rates, we used a microlite number density (*Nv*) exsolution rate meter (MND; Toramaru et al., 2008) for plagioclase microlites present in microlite-poor pyroclasts (e.g. Cimarelli et al., 2010) (see Supp. Material 1 for details). The resulting velocities (Table 4) are higher for LU1.2 and LU1.6, being 0.43 and 0.30 m s^{-1}, respectively. Contrastingly, LU1.4 and LU2.1 show respective velocities of 0.21 and 0.17 m s^{-1}. The lower velocities measured from LU2.1 are coherent with 10 h of eruptive pause on 27 September. These are also consistent with the longest phenocryst crystallization times (up to 65 h; Table 1) and may indicate that the rapid empting of the shallower system may have led to longer residence of the magma in the reservoir. Accordingly, we consider our faster velocities achieved in LU1.2 and LU1.6 are reasonable with magma acceleration and fragmentation in the conduit (e.g., Cimarelli et al., 2010), and lower magma viscosities before the collapse. These rates (Table 4) are in agreement with the development of an intense hybrid eruption phase. Comparatively, the 2014–2015 Holuhraun eruption (Iceland) basaltic magma had similar ascent rate of 0.12–0.29 m s^{-1} (Hartley et al., 2018).

Our direct observations, video footage and thermal imaging, suggests the collapse did not dramatically modify the eruption style on a timescale of hours to days, although a shorter-term (minutes to hours) impact was documented. Particularly, during the flank collapse, lava overflow indicated an increase of the lava effusion. Also, direct observations describe two closely spaced lava fountains on 25 September, in contrast to the pre-collapse situation when the explosive activity was focalized in the main vent. Previous research has reported vent migration and a new arrangement of dikes soon after a wide range of volcanic lateral collapse sizes as a direct response to stress-strain modifications (e.g., Maccaferri et al., 2017; Tibaldi et al., 2008; Shevchenko et al., 2020).

Table 4
Crystal fraction (ϕ), number density (N_A, Eq.2), mean crystal size (*Sm*, Eq. 3) and volumetric number density (*Nv*), the nucleation depth (*Dpw/dz*, Eq. 4), vesicularity (Ves %), density of the bubbly magma ρ, and ascent velocities (V_n, Eq. 5) for crystal populations. The density of the bubbly magma is obtained as: $\rho = \rho_m \times (1 - f)$, being ρ_m the magma density (assumed 2700 kg m-3) and *f* the vesicle fraction measured from BSE images.

Sample	Φ	N_A	S_m (um)	N_V (mm^{-3})	CSi	ΔC_{Si}	Cw	c	a	Dpw/dz	% Ves	ρ bubbly magma	V_n (m s^{-1})	V_n km/h
LU1.2	13.2	4.04E+03	5.72	7.07E+05	47.26	−2.74	2.2	2.46E+07	1.3E+14	3.57	0.69	837	0.49	1.77
LU1.4	13.0	7.54E+03	4.18	1.80E+06	46.70	−3.30	2.1	2.35E+07	9.4E+13	2.66	0.79	567	0.21	0.74
LU1.6	11.3	3.92E+03	5.81	6.74E+05	45.61	−4.39	2.0	2.24E+07	4.6E+13	4.43	0.58	1134	0.30	1.10
LU2.1	16.8	2.49E+03	7.29	3.40E+05	46.15	−3.85	2.2	2.46E+07	5.2E+13	2.62	0.72	756	0.17	0.63

4.4. Implications for volcanic hazard

The complex chain of events described in this contribution has several implications for volcanic hazards. First, eruption styles allowing rapid pyroclastic accumulations around the vent (e.g., intense Strombolian activity or lava fountaining) can rapidly favor the formation of hot and deformable deposits. Second, the cessation and reactivation of lava flows that penetrate the edifice flanks (in the form of lava seeps) can also destabilize the cone. Rapid changes in the magmatic activity may be responsible for both the edifice breaching and sudden lava overflows to lower elevations. Third, the lateral collapse occurred during the period of most intense eruptive activity since the beginning of the eruption and was only preceded by smaller landslides, without any other precursory signals. In this respect, we should consider these periods of highest eruption rates as effective triggering factors for the collapse of rapidly growing cones formed over steep surfaces. The edifice failure also results in a dramatic change in the morphology of the cone and the distribution of the lava flows in the coming days. The large, rafted blocks carried by the lava flows may enhance their mechanical impact and hazard potential. In the Tajogaite 2021 eruption, they also created a temporary natural barrier to flows draining to the S, at least during this phase of the eruption, and lava drained exclusively to the N and affected other inhabited areas. The change in the pattern of lava drainage is difficult to assess in real-time through lava flow modeling. A detailed study is required to understand the rheological behavior of these raft-bearing lavas, and how their emplacement may impact the distribution of subsequent lava flows. Finally, collapse-induced eruptive changes, which are not clearly identified in this study, but which have been reported before for similar collapses of small volcanoes (Németh et al., 2011; Romero et al., 2020) may lead to enhanced blast or explosive activity hazards, including vent changes induced by flank collapse. As a consequence, lateral collapses during cone-forming eruptions represent a notable hazard by their nature, dimensions, and dynamics; they can represent a high risk due to higher vulnerability of infrastructure when occurring in the vicinity of populated areas, but also for volcanologists documenting these eruptions.

5. Concluding remarks

The multidisciplinary study of the first phase of the 2021 eruption of Tajogaite cone has provided critical insights into the eruption evolution and cone growth-destruction. In particular, we found that:

1) The real-time monitoring of the 2021 eruption of the Tajogaite cone in the Cumbre Vieja ridge (La Palma), together with the forensic reconstruction of its deposits, provides a unique asset of observations to reconstruct the cone-forming volcanic activity and the 25 September lateral collapse. This information represents a powerful complement to geologic observations that describe the interplay between constructive and destructive processes in other small-volume volcanoes.
2) The lateral collapse on 25 September affected the W flank of the edifice. Both the steep slope of the pre-eruptive surface and the rapid accumulation of pyroclasts conditioned the gravitational instability of the edifice. Ultimately, the rapid pyroclastic accumulation and the reactivation of the SW lava flow triggered the collapse, which coincides with the direction of the inclined dike feeding the eruption. The event started as a lava overflow in the base of the cone towards the SW, which acted as a deforming substrate (lava seep) to produce spreading and rotational rockslide at minimum speeds of 34 to 70 m h^{-1}. The edifice morphology resulted in a U-shaped scar, and proximal megablocks covered a significant area downslope in the collapse direction, as well post-collapse raft-bearing lavas drained towards the SW.
3) The textural investigation of pyroclastic products evidences intense lava fountaining both which preceded and accompanied the collapse, whereas Strombolian behavior characterized the beginning and late first stage of the eruption. Also, the highest tephra discharge rates were achieved shortly before and during the collapse event. This is also supported by conduit dynamics indicating the highest magma ascent rates (0.30 m s^{-1}) and shorter crystallization times for microlites during that period of time.
4) The nature and development of the 25 September event suggest that lateral collapses in newly formed small-volume edifices may occur without warning and result in dramatic transformations of their morphology and the surrounding landscape. Especially for populations living nearby these growing volcanoes, it constitutes a high threat that must be considered for volcanic hazard assessment and risk mitigation. Finally, yet importantly, the volcanologists present on the field must also have great caution when operating in the areas closest to fast-growing cones, whose partial collapse can pose sudden hazards from pyroclastic density currents and related phenomena.

Supplementary data to this article can be found online at https://doi.org/10.1016/j.jvolgeores.2022.107642.

CRediT authorship contribution statement

Jorge E. Romero: Visualization, Formal analysis, Investigation, Data curation, Writing – original draft. **Mike Burton:** Formal analysis, Investigation, Writing – review & editing. **Francisco Cáceres:** Investigation, Formal analysis, Writing – original draft, Writing – review & editing. **Jacopo Taddeucci:** Investigation, Formal analysis, Writing – original draft, Writing – review & editing. **Riccardo Civico:** Investigation, Formal analysis, Writing – original draft, Writing – review & editing. **Tullio Ricci:** Investigation, Formal analysis, Writing – original draft, Writing – review & editing. **Matthew J. Pankhurst:** Formal analysis, Investigation, Writing – review & editing. **Pedro A. Hernández:** Formal analysis, Investigation, Writing – review & editing. **Costanza Bonadonna:** Formal analysis, Investigation, Writing – review & editing. **Edward W. Llewellin:** Formal analysis, Investigation, Writing – review & editing. **Marco Pistolesi:** Formal analysis, Investigation, Writing – review & editing. **Margherita Polacci:** Writing – original draft, Writing – review & editing. **Carmen Solana:** Formal analysis, Investigation, Writing – review & editing. **Luca D'Auria:** Formal analysis. **Fabio Arzilli:** Writing – original draft, Writing – review & editing. **Daniele Andronico:** Formal analysis, Investigation, Writing – review & editing. **Fátima Rodríguez:** Formal analysis. **Maria Asensio-Ramos:** Formal analysis, Investigation, Writing – review & editing. **Alba Martín-Lorenzo:** Formal analysis. **Catherine Hayer:** Formal analysis. **Piergiorgio Scarlato:** Formal analysis, Investigation, Writing – review & editing. **Nemesio M. Perez:** Formal analysis.

Declaration of Competing Interest

The authors declare that they have no known competing financial interests or personal relationships that could have appeared to influence the work reported in this paper.

Data availability

Data will be made available on request.

Acknowledgements

We are grateful to Instituto Volcanológico de Canarias (INVOLCAN), who allowed and supported our field activities during the crisis. Fieldwork was financed through NSFGEONERC-funded project DisEqm (NERC Reference: NE/N018575/1; NE/N018443/1) and V-PLUS projects. Other funding was provided by VOLRISKMAC (MAC/3.5b/124), VOLRISKMAC II (MAC2/3.5b/328) and LPvolcano (Cabildo de La Palma) projects. FC acknowledges funding from the Deutsche

Forschungsgemeinschaft (DFG - German Research Foundation) through the project n° 457579444 (CA 2743/1-1). This contribution is part of JER PhD, supported through a Dean's Doctoral Scholar Awards of the University of Manchester. We thank Lewis Hughes and Thomas Bishop for handling and support with the Quanta 650 ESEM and Rigaku NEX-CG Energy Dispersive XRF analyses. We are grateful to José Barrancos, Ana Pardo, Germán Padilla, Samantha Tramontano and Iván Cabrera for their assistance in the field. The reviews from Prof. K. Németh, an anonymous reviewer and Editor Dr. Sonia Calvari are greatly appreciated. These instruments belong to the Williamson Research Centre Mineral Analysis Facility and the Arthur Lewis Building Geography Laboratories of the University of Manchester.

References

Abdel-Monem, A., Watkins, N., Gast, P.W., 1972. Potassium-argon ages, volcanic stratigraphy, and geomagnetic polarity history of the Canary Islands; Tenerife, La Palma and Hierro. Am. J. Sci. 272 (9), 805–825.

Acocella, V., 2005. Modes of sector collapse of volcanic cones: Insights from analogue experiments. J. Geophys. Res. Solid Earth 110 (B2).

Andrade, S.D., van Wyk de Vries, B., 2010. Structural analysis of the early stages of catastrophic stratovolcano. Bull. Volcanol. 72 (7), 771–789.

Andronico, D., Behncke, B., De Beni, E., Cristaldi, A., Scollo, S., Lopez, M., Lo Castro, M. D., 2018a. Magma Budget from Lava and Tephra Volumes Erupted during the 25-26 October 2013 Lava Fountain at Mt Etna. Front. Earth Sci. 6, 116.

Andronico, D., Di Roberto, A., De Beni, E., Behncke, B., Bertagnini, A., Del Carlo, P., Pompilio, M., 2018b. Pyroclastic density currents at Etna volcano, Italy: the 11 February 2014 case study. J. Volcanol. Geotherm. Res. 357, 92–105.

Apuani, T., Corazzato, C., Cancelli, A., Tibaldi, A., 2005a. Physical and mechanical properties of rock masses at Stromboli: a dataset for volcano instability evaluation. Bull. Eng. Geol. Environ. 64 (4), 419–431.

Apuani, T., Corazzato, C., Cancelli, A., Tibaldi, A., 2005b. Stability of a collapsing volcano (Stromboli, Italy): limit equilibrium analysis and numerical modelling. J. Volcanol. Geotherm. Res. 144 (1–4), 191–210.

Arzilli, F., Agostini, C., Landi, P., Fortunati, A., Mancini, L., Carroll, M.R., 2015. Plagioclase nucleation and growth kinetics in a hydrous basaltic melt by decompression experiments. Contrib. Mineral. Petrol. 170 (5), 1–16.

Arzilli, F., La Spina, G., Burton, M.R., Polacci, M., Le Gall, N., Hartley, M., Di Genova, D., Cai, B., Vo, N.T., Bamber, E.C., Nonni, S., Atwood, R., Llewellin, E., Brooker, R.A., Mader, H.M., Lee, P.D., 2019. Magma fragmentation in highly explosive basaltic eruptions induced by rapid crystallization. Nat. Geosci. 12 (12), 1023–1028.

Báez, W., Carrasco-Nuñez, G., Giordano, G., Viramonte, J.G., Chiodi, A., 2016. The polycyclic scoria Cones of the Antofagasta de la Sierra basin, Southern Puna Plateau, Argentina. In: Németh, K., Carrasco-Núñez, G., JJY, Aranda-Gómez, IEM, Smith (Eds.), Monogenetic Volcanism, 446. GSA Special Publications, pp. 311–336.

Bamber, E.C., Arzilli, F., Polacci, M., Hartley, M., Fellowes, J., Di Genova, D., Chavarría, D., Saballos, J.A., Burton, M.R., 2020. Pre-and syn-eruptive conditions of a basaltic Plinian eruption at Masaya Volcano, Nicaragua: the Masaya Triple Layer (2.1 ka). J. Volcanol. Geotherm. Res. 392, 106761.

Barker, A.K., Troll, V.R., Carracedo, J.C., Nicholls, P.A., 2015. The magma plumbing system for the 1971 Teneguía eruption on La Palma, Canary Islands. Contrib. Mineral. Petrol. 170 (5), 1–21.

Behncke, B., Calvari, S., Giammanco, S., Neri, M., Pinkerton, H., 2008. Pyroclastic density currents resulting from the interaction of basaltic magma with hydrothermally altered rock: an example from the 2 006 summit eruptions of Mount Etna, Italy. Bull. Volcanol. 70 (10).

Bonadonna, C., Costa, A., 2012. Estimating the volume of tephra deposits: a new simple strategy. Geology 40 (5), 415–418.

Brown, R.J., Thordarson, T., Self, S., Blake, S., 2015. Disruption of tephra fall deposits caused by lava flows during basaltic eruptions. Bull. Volcanol. 77 (10), 1–15.

Brugger, C., Hammer, J., 2010. Crystal size distribution analysis of plagioclase in experimentally decompressed hydrous rhyodacite magma. Earth Planet. Sci. Lett. 300, 246–254.

Calvari, S., Intrieri, E., Di Traglia, F., Bonaccorso, A., Casagli, N., Cristaldi, A., 2016. Monitoring crater-wall collapse at active volcanoes: a study of the 12 January 2013 event at Stromboli. Bull. Volcanol. 78 (5), 39.

Carracedo, J.C., Day, S., Guillou, H., Rodríguez Badiola, E., Canas, J.A., Pérez Torrado, F. J., 1998. Hotspot volcanism close to a passive continental margin: the Canary Islands. Geol. Mag. 135 (5), 591–604.

Carracedo, J.C., Rodriguez-Badiola, E., Guillou, H., de la Nuez, J., Pérez Torrado, F.J., 2001. Geology and volcanology of la Palma and el Hierro, western Canaries. Estud. Geol. 57, 175–273.

Carracedo, J.C., Troll, V.R., Day, J.M., Geiger, H., Aulinas, M., Soler, V., Deegan, F.M., Pérez-Torrado, J., Gisbert, G., Gazel, E., Rodríguez-González, A., Albert, E., 2022. The 2021 eruption of the Cumbre Vieja Volcanic Ridge on La Palma, Canary Islands. Geol. Today 38 (3), 94–107.

Casagli, N., Tibaldi, A., Merri, A., Del Ventisette, C., Apuani, T., Guerri, L., Fortuny-Guasch, J., Tarchi, D., 2009. Deformation of Stromboli Volcano (Italy) during the 2007 eruption revealed by radar interferometry, numerical modelling and structural geological field data. J. Volcanol. Geotherm. Res. 182 (3–4), 182–200.

Cashman, K.V., 2020. Crystal size distribution (CSD) analysis of Volcanic samples: advances and challenges. Front. Earth Sci. 8, 291.

Casillas, R., de la Nuez, J., Fernández Rodríguez, C., Colmenero Navarro, J.R., Jourdan, F., Harangi, S., Lukács, R., 2020. Edad de las rocas volcánicas submarinas y plutónicas del Complejo Basal de La Palma: implicaciones en la evolución geológica temprana de la isla. Geogaceta 67, 47–50.

Castro, J.M., Feisel, Y., 2022. Eruption of ultralow-viscosity basanite magma at Cumbre Vieja, La Palma, Canary Islands. Nat. Commun. 13, 3174.

Cimarelli, C., Di Traglia, F., Taddeucci, J., 2010. Basaltic scoria textures from a zoned conduit as precursors to violent Strombolian activity. Geology 38 (5), 439–442.

Civico, R., Ricci, T., Scarlato, P., Taddeucci, J., Andronico, D., Del Bello, E., D'Auria, L., Hernández, P.A., Pérez, N.M., Asensio-Ramos, M., Barrancos, J., Calvo, D., Martínez van Dorth, D., Padrón, E., Álvarez, A., Doglioni, C., 2022. 2021 Cumbre Vieja volcano eruption (La Palma, Spain) SfM DSM, Sep 2021. Distributed by OpenTopography.

Civico, R., Ricci, T., Scarlato, P., Taddeucci, J., Andronico, D., Del Bello, E., D'Auria, L., Hernández, P., Pérez, N.M., 2022a. High-resolution Digital Surface Model of the 2021 eruption deposit of Cumbre Vieja volcano, La Palma, Spain. Scientific Data 9, 435.

Cutler, K.S., Watt, S.F., Cassidy, M., Madden-Nadeau, A.L., Engwell, S.L., Abdurrachman, M., Nurshal, M.E.M., Tappin, D.R., Carey, S., Novellino, A., Hayer, C., Hunt, J.E., Day, S.J., Grilli, S.T., Kurniawan, I.A., Kartadinata, N., 2022. Downward-propagating eruption following vent unloading implies no direct magmatic trigger for the 2018 lateral collapse of Anak Krakatau. Earth Planet. Sci. Lett. 578, 117332.

Daggitt, M.L., Mather, T.A., Pyle, D.M., Page, S., 2014. AshCalc–a new tool for the comparison of the exponential, power-law and Weibull models of tephra deposition. J. Appl. Volcanol. 3 (1), 7.

D'Auria, L., Koulakov, I., Prudencio, J., Cabrera-Pérez Ibanez, J., Barrancos, J., García-Hernández, R., Martínez van Dorth, D., Padilla Hernández, G., Przeor, M., Ortega, V., Hernández, P., Pérez, N., 2022. Voluminous storage and rapid magma ascent beneath La Palma revealed by seismic tomography. Sci. Rep. Preprint at: Submitted for publication https://assets.researchsquare.com/files/rs-1238072/v1/f2753174-18eb-4e0d-8ec0-3f762489e3aa.pdf?c=1642088387.

Day, S.J., Carracedo, J.C., Guillou, H., Pais Pais, F.J., Rodríguez Badiola, E., Fonseca, J.F. B.D., Heleno, S.N.I., 2000. Comparison and cross-checking of historical, archaeological and geological evidence for the location and type of historical and sub-historical eruptions of multiple-vent oceanic island volcanoes. Geol. Soc. Lond. Spec. Publ. 171, 281–306.

De Luca, C., Valerio, E., Giudicepietro, F., Macedonio, G., Casu, F., Lanari, R., 2022. Pre- and co-eruptive analysis of the September 2021 Eruption at Cumbre Vieja Volcano (La Palma, Canary Islands) through DInSAR measurements and analytical modeling. Geophys. Res. Lett. 49 (7) e2021GL097293.

Filipovich, R., Báez, W., Bustos, E., Villagrán, A., Chiodi, A., Viramonte, J.G., 2019. Estilos eruptivos asociados al volcaismo monogenético máfico de la región de Pasto Ventura, Puna Austral, Argentina. Andean Geol. 46 (2), 300–335.

Giordano, D., Russell, J.K., Dingwell, D.B., 2008. Viscosity of magmatic liquids: a model. Earth Planet. Sci. Lett. 271 (1–4), 123–134.

González, P.J., 2022. Volcano-tectonic control of Cumbre Vieja. Science 375 (6587), 1348–1349.

Guillou, H., Carracedo, J.C., Day, S.J., 1998. Dating of the upper Pleistocene–Holocene volcanic activity of La Palma using the unspiked K–Ar technique. J. Volcanol. Geotherm. Res. 86 (1–4), 137–149.

Hartley, M.E., Bali, E., Maclennan, J., Neave, D.A., Halldórsson, S.A., 2018. Melt inclusion constraints on petrogenesis of the 2014–2015 Holuhraun eruption, Iceland. Contrib. Mineral. Petrol. 173, 10.

Hightower, E., 2016. Clastogenesis as a result of Reactivation of Agglutinated Spatter. Learning Science through Research. KECK Geology Consortium, 29th Annual Symposium, Short Contributions, p. 6.

Holm, R.F., 1987. Significance of agglutinate mounds on lava flows associated with monogenetic cones: an example at Sunset Crater, northern Arizona. Geol. Soc. Am. Bull. 99 (3), 319–324.

Houghton, B.F., Taddeucci, J., Andronico, D., Gonnermann, H.M., Pistolesi, M., Patrick, M.R., Orr, T.R., Swanson, D.A., Edmonds, M., Gaudin, D., Carey, R.J., Scarlato, P., 2016. Stronger or longer: Discriminating between Hawaiian and Strombolian eruption styles. Geology 44 (2), 163–166.

Hungr, O., Leroueil, S., Picarelli, L., 2014. The Varnes classification of landslide types, an update. Landslides 11 (2), 167–194.

Kaneko, T., Maeno, F., Ichihara, M., Yasuda, A., Ohminato, T., Nogami, K., Nakada, S., Honda, Y., Murakami, H., 2022. Episode 4 (2019–2020) Nishinoshima activity: abrupt transitions in the eruptive style observed by image datasets from multiple satellites. Earth, Planets Space 74 (1), 1–23.

Kereszturi, G., Németh, K., 2012. Monogenetic basaltic olcanoes: Genetic classification, growth, geomorphology and degradation. In: Németh, K. (Ed.), Updates in Volcanology—New Advances in Understanding Volcanic Systems. InTech Open, Rijeka, Croatia, pp. 3–89.

Klügel, A., Hoernle, K.A., Schmincke, H.U., White, J.L., 2000. The chemically zoned 1949 eruption on La Palma (Canary Islands): petrologic evolution and magma supply dynamics of a rift- zone eruption. J. Geophys. Res. 105 (B3), 5997–6016.

Kovalenko, V.I., Naumov, V.B., Girnis, A.V., Dorofeeva, V.A., Yarmolyuk, V.V., 2007. Volatiles in basaltic magmas of ocean islands and their mantle sources: I. Melt compositions deduced from melt inclusions and glasses in the rocks. Geochem. Int. 45 (2), 105–122.

Le Bas, M., Maitre, R.L., Streckeisen, Zanettin, B., 1986. A chemical classification of volcanic rocks based on the total alkali-silica diagram. J. Petrol. 27 (3), 745–750.

Longpré, M.A., Felpeto, A., 2021. Historical volcanism in the Canary Islands; part 1: a review of precursory and eruptive activity, eruption parameter estimates, and implications for hazard assessment. J. Volcanol. Geotherm. Res. 107363.

Luhr, J.F., Simkin, T., 1993. Parícutin, the Volcano Born in a Mexican Cornfield. Geoscience Press, Inc., Pheonix, p. 427.
Maccaferri, F., Richter, N., Walter, T.R., 2017. The effect of giant lateral collapses on magma pathways and the location of volcanism. Nat. Commun. 8 (1), 1–11.
Mannen, K., Ito, T., 2007. Formation of scoria cone during explosive eruption at Izu-Oshima volcano, Japan. Geophys. Res. Lett. 34 (18).
Marín, C., Rodríguez, I., Godoy, B., et al., 2020. Eruptive history of La Poruña scoria cone, Central Andes, Northern Chile. Bull. Volcanol. 82 (11), 1–19.
McGetchin, T.R., Chouet, B.A., 1974. Cinder cone growth modeled after northeast crater, Mount Etna, Sicily. J. Geophys. Res. 79 (23), 3257–3272.
Neave, D.A., Putirka, K.D., 2017. A new clinopyroxene-liquid barometer, and implications for magma storage pressures under Icelandic rift zones. Am. Mineral. 102 (4), 777–794.
Németh, K., Risso, C., Nullo, F., Kereszturi, G., 2011. The role of collapsing and cone rafting on eruption style changes and final cone morphology: Los Morados scoria cone, Mendoza, Argentina. Open Geosci. 3 (2), 102–118.
Norini, G., De Beni, E., Andronico, D., Polacci, M., Burton, M., Zucca, F., 2008. The 16 November 2006 flank collapse of South-East Crater at Mount Etna, Italy: study of the deposit and hazard assessment. J. Geophys. Res. 109.
Padrón, E., Pérez, N.M., Melián, G.V., Sumino, H., Mar, A., Recio, G., Asensio-Ramos, M., Rodríguez, F., D'Auria, L., 2021. Temporal evolution of $^{3}He/^{4}He$ isotopic ratio at Dos Aguas Cold Mineral Spring, La Palma, Canary Islands. In EGU General Assembly Conference Abstracts (pp. EGU21-14994).
Pankhurst, M.J., et al., 2022. Rapid response petrology for the opening eruptive phase of the 2021 Cumbre Vieja eruption, La Palma, Canary Islands. Volcanica 5 (1), 1–10. https://doi.org/10.30909/vol.05.01.0110.
Patrick, M.R., Orr, T.R., 2012. Rootless shield and perched lava pond collapses at Kīlauea Volcano, Hawai'i. Bull. Volcanol. 74 (1), 67–78.
Polacci, M., Baker, D.R., Bai, L., Mancini, L., 2008. Large vesicles record pathways of degassing at basaltic volcanoes. Bull. Volcanol. 70 (9), 1023–1029.
Polacci, M., Burton, M.R., La Spina, A., Muré, F., Favretto, S., Zanni, F., 2009. The role of syn-eruptive vesiculation on explosive basaltic activity at Mt. Etna, Italy. J. Volcanol. Geotherm. Res. 179 (3–4), 265–269.
Presta, J.F., Caffe, P.J., 2014. Historia evolutiva de los volcanes monogenéticos El Toro (23°05'S-66°42'W), Puna norte, Argentina. Andean Geol. 41 (1), 142–173.
Putirka, K.D., 2005. Mantle potential temperatures at Hawaii, Iceland, and the mid-ocean ridge system, as inferred from olivine phenocrysts: evidence for thermally driven mantle plumes. Geochem. Geophys. Geosyst. 6 (5).
Putirka, K.D., 2008. Thermometers and barometers for volcanic systems. Rev. Mineral. Geochem. 69 (1), 61–120.
Riggs, N.R., Duffield, W.A., 2008. Record of complex scoria cone eruptive activity at Red Mountain, Arizona, USA, and implications for monogenetic mafic volcanoes. J. Volcanol. Geotherm. Res. 178 (4), 763–776.
Riker, J.M., Cashman, K.V., Rust, A.C., Blundy, J.D., 2015. Experimental Constraints on Plagioclase Crystallization during H_2O- and H_2O–CO_2 -Saturated Magma Decompression. J. Petrol. 56 (10), 1967–1998.
Romero, C., Galindo, I., Sánchez, N., Martín-González, E., Vegas, J., 2020. Syn-eruptive lateral collapse of monogenetic volcanoes: the case of mazo volcano from the timanfaya eruption (Lanzarote, Canary Islands). In: Nemeth, K. (Ed.), Volcanoes-Updates in Volcanology. BoD – Books on Demand, Germany.
Romero, J.E., Polacci, M., Watt, S., Kitamura, S., Tormey, D., Sielfeld, G., Arzilli, F., La Spinna, G., Franco, L., Burton, M., Polanco, E., 2021. Volcanic lateral collapse processes in Mafic Arc Edifices: a review of their driving processes, types and consequences. Front. Earth Sci. 9, 639825.
Romero, J.E., Ureta, G., Fuentes, P., Corgne, A., Naranjo, J.A., Ramírez, C., Chako-Tchamabé, B., Cáceres, M., Lazcano, J., 2022. The eruptive history and magma composition of Pleistocene Cerro Negro volcano (Northern Chile): Implications for the complex evolution of large monogenetic volcanoes. J. Volcanol. Geotherm. Res. 429, 107618.
Shea, T., Hammer, J.E., 2013. Kinetics of cooling-and decompression-induced crystallization in hydrous mafic-intermediate magmas. J. Volcanol. Geotherm. Res. 260, 127–145.
Shevchenko, A.V., et al., 2020. The rebirth and evolution of Bezymianny volcano, Kamchatka after the 1956 sector collapse. Commun. Earth Environ. 1 (1), 1–15. https://doi.org/10.1038/s43247-020-00014-5.
Stewart, R., Németh, K., 2009. Evidence of multiple scoria cones and cone collapse at Pouerua Volcano, Northland volcanic field, New Zealand. Geol. Soc. New Zealand Miscell. Public. 128A, 203.
Sumner, J.M., 1998. Formation of clastogenic lava flows during fissure eruption and scoria cone collapse: the 1986 eruption of Izu-Oshima Volcano, eastern Japan. Bull. Volcanol. 60 (3), 195–212.
Tibaldi, A., Corazzato, C., Kozhurin, A., Lagmay, A.F.M., Pasquare, F.A., Ponomareva, V. V., Rust, D., Tormey, D., Vezzoli, L., 2008. Influence of substrate tectonic heritage on the evolution of composite volcanoes: predicting sites of flank eruption, lateral collapse, and erosion. Glob. Planet. Chang. 61 (3–4), 151–174.
Toramaru, A., Noguchi, S., Oyoshihara, S., Tsune, A., 2008. MND (microlite number density) water exsolution rate meter. J. Volcanol. Geotherm. Res. 175 (1–2), 156–167.
Torres-González, P.A., Luengo-Oroz, N., Lamolda, H., Alessandro, W.D., Albert, H., Iribarren, I., Moure-García, D., Soler, V., 2020. Unrest signals after 46 years of quiescence at Cumbre Vieja, La Palma, Canary Islands. J. Volcanol. Geotherm. Res. 392, 106757.
Valentine, G.A., Gregg, T.K.P., 2008. Continental basaltic volcanoes—processes and problems. J. Volcanol. Geotherm. Res. 857–873.
Valentine, G.A., Krier, D., Perry, F.V., Heiken, G., 2005. Scoria cone construction mechanisms, Lathrop Wells volcano, southern Nevada, USA. Geology 33 (8), 629–632.
Valentine, G.A., Perry, F.V., Krier, D., Keating, G.N., Kelley, R.E., Cogbill, A.H., 2006. Small-volume basaltic volcanoes: Eruptive products and processes, and posteruptive geomorphic evolution in Crater flat (Pleistocene), southern Nevada. Geol. Soc. Am. Bull. 118 (11–12), 1313–1330.
Vona, A., Romano, C., Dingwell, D.B., Giordano, D., 2011. The rheology of crystal-bearing basaltic magmas from Stromboli and Etna. Geochim. Cosmochim. Acta 75 (11), 3214–3236.
Weis, F.A., Skogby, H., Troll, V.R., 2015. Magmatic water contents determined through clinopyroxene: examples from the Western Canary Islands, Spain. Geochem. Geophys. Geosyst. 16 (7), 2127–2146.
Williams, R.S., Moore, J.G., 1983. Man against Volcano: The Eruption on Heimaey, Vestmannaeyjar. Geological Survey Publication, Iceland. U.S, p. 33.
Wood, C.A., 1980. Morphometric evolution of cinder cones. J. Volcanol. Geotherm. Res. 7 (3–4), 387–413.
Younger, Z.P., Valentine, G.A., Gregg, T.K., 2019. A'ā lava emplacement and the significance of rafted pyroclastic material: Marcath volcano (Nevada, USA). Bull. Volcanol. 81 (9), 1–15.
Zellmer, G.F., 2021. Gaining acuity on crystal terminology in volcanic rocks. Bull. Volcanol. 83 (11), 1–8.